

A SEARCH FOR LIGHTLY IONIZING PARTICLES
IN THE LUX DETECTOR AND R&D FOR FUTURE
EXPERIMENTS

by

KATAYUN J KAMDIN

A dissertation submitted in partial satisfaction of the
requirements for the degree of

Doctor of Philosophy

in

Physics

in the

Graduate Division

of the

University of California, Berkeley

Committee in charge:

Professor Daniel McKinsey, Chair

Professor Marjorie Shapiro

Doctor Peter Sorensen

Professor Kai Vetter

Summer 2018

ABSTRACT

A Search for Lightly Ionizing Particles in the LUX Detector and R&D
For Future Experiments

by

Katayun J Kamdin

Doctor of Philosophy
University of California, Berkeley
Professor Daniel McKinsey, Chair

Write the abstract here.

To my mom, for always making me feel like I could do this. To my friends, for being there when I was sure I couldn't.

ACKNOWLEDGMENTS

Some Text

More Text.

More text

CONTENTS

1	INTRODUCTION	1
I	THEORETICAL CONTEXT AND EXPERIMENTAL STRATEGIES	2
2	THEORETICAL BACKGROUND	3
2.1	A Little History	3
2.2	The Standard Cosmology	3
2.3	Evidence for Dark Matter	4
2.3.1	Galaxies and Clusters	4
2.3.2	Cosmic Microwave Background	4
2.4	Dark Matter Candidates Motivated by Particle Physics	4
2.4.1	WIMPS and the Hierarchy Problem	4
2.4.2	Axions and the Strong CP Problem	4
2.5	Motivation for LIPs	4
2.6	Experimental Strategies for Detecting Dark Matter	4
2.6.1	Production	4
2.6.2	Indirect Detection	4
2.6.3	Direct Detection	4
3	PARTICLE DETECTION WITH LIQUID XENON	5
3.1	Liquid Xenon as a Detector Medium	5
3.1.1	Properties of Liquid Xenon	5
3.1.2	Scintillation and Ionization Signal Generation	7
3.2	Dual-Phase Xenon Time Projection Chamber	8
3.2.1	Energy Reconstruction	10
3.3	Dual-Phase Xenon TPCs for Dark Matter Detection	12
3.3.1	WIMP Searches with LXe TPCs	13
3.3.2	Other Dark Matter Searches with LXe TPCs	16
II	BIG SCIENCE	22
4	THE LUX DETECTOR	23
4.1	Detector Components	23
4.1.1	Cryostat	23
4.1.2	PMTs	23
4.1.3	Water Tank	23
4.1.4	Trigger and Data Acquisition	23
4.2	Calibrations	23
4.2.1	Energy	23
4.2.2	Tritium	24
4.2.3	DD	24
4.2.4	Kr	24

5	LIGHTLY IONIZING PARTICLE SEARCH	25
5.1	Modeling LIP Interaction	25
5.1.1	Collision Cross Section	25
5.1.2	Photo Absorption Ionization Model for Charge Particle Energy Loss	26
5.1.3	Straggling	27
5.1.4	Energy Resolution in LUX	27
5.1.5	Position Resolution in LUX	27
5.2	LIP Search	27
5.2.1	LUX Run03 Conditions	27
5.3	LIP Search Analysis	27
5.3.1	Energy Consistency	27
5.3.2	Track Linearity Criteria	27
5.3.3	Background Rejection	27
5.3.4	Muons	27
5.3.5	Gammas	27
5.3.6	Electron Trains?	27
5.4	Result: Vertical Flux Limit	27
III	LITTLE SCIENCE	28
6	RESEARCH AND DEVELOPMENT FOR FUTURE LXE TPCS	29
6.1	Test Bed Apparatus Overview	29
6.2	Circulation System	31
6.3	Charge Amplifiers	31
6.3.1	Charge Amplifier Noise Behavior	33
6.4	PMT	35
6.5	Slow Control	35
6.6	Data Acquisition	36
6.7	High Voltage Feedthrough Design	36
6.7.1	Implementing SHV Feed Throughs from Vac- uum Suppliers	37
6.7.2	Custom Feedthroughs	43
7	SOLUBILITY OF RADON DAUGHTERS IN LIQUID XENON	47
7.1	Motivation	47
7.1.1	Plate Out	49
7.2	Experimental Configuration and Method	50
7.2.1	Plate Out of ^{220}Rn Daughters	52
7.2.2	Data Collection	53
7.2.3	Calibration	54
7.2.4	Position Reconstruction	54
7.2.5	Fiducial Volume	55
7.3	Analysis	55
7.3.1	Number of ^{220}Rn daughters in the TPC	55

7.3.2	Data Selection	55
7.4	Results and Discussion	58
8	ELECTRON TRAIN STUDIES	66
8.1	Electron Train Studies	66
8.1.1	Motivation	66
8.1.2	Experimental Configuration	66
8.1.3	Results	66
IV	APPENDIX	67
A	DUMMY APPENDIX	68
	BIBLIOGRAPHY	69

LIST OF FIGURES

Figure 1	(left) Diagram of a dual-phase xenon time projection chamber. The time difference between S1 and S2 gives the depth (z) of the interaction, and (x, y) is reconstructed from the S2 signal. (right) Diagram summarizing the generation of the scintillation and ionization signal generation in dual-phase xenon time projection chambers.	9
Figure 2	(left) Plot illustrating the effect of recombination and detector effects on a line source (^{127}Xe), courtesy of E. Pease. (right) Field dependence of scintillation and ionization yield in LXe for 122 keV electron recoils (ER), 56.5 keV nuclear recoils (NR) and 5.5 MeV alphas, relative to the yield with no drift field from [11]	11
Figure 3	Plots showing combined energy contours in two common sets of axis units, for an example set of g_1 and g_2 .	12
Figure 4	Plot showing ER and NR bands from LUX. Solid lines are the ER and NR Gaussian means μ , dotted lines are $\mu \pm 1\sigma$. Figure from [10]	13
Figure 5	Plot showing spin-independent WIMP rates in common detector target materials, dots indicate typical thresholds for the targets. Xenon gains in favored SUSY parameter space ($M_\chi \gtrsim 100 \text{ GeV}$) due to a kinematic enhancement ($M_\chi \sim M_{Xe}$) and a cross-section enhancement ($\sigma_{SI} \propto A^2$). Figure from [17]	17
Figure 6	Projected limits of next-generation dark matter detectors and areas where SUSY models predict the presence of WIMPs. Although Xe (LZ, green dashed) performs better for WIMP parameter space, Ge and Si (SuperCDMS, blue dashed) can access other light dark matter parameter space below 10 GeV. The plot was generated by http://dmtools.brown.edu/	17
Figure 7	Xenon 10 low-mass WIMP limit extended the range of the standard WIMP result.	19

Figure 8	(left) Top: Expected 1,2,3-electron signal rates for Sub-GeV DM with $\sigma_e = 10^{-36} \text{ cm}^2$ and Bottom: exclusion limit set with Xenon10 few-electron signals. (right) Exclusion limits for dark matter scattering through an electric-dipole moment (red) and through a very light ($\ll \text{keV}$) mediator (blue)	19
Figure 9	(left) Recent limits on solar axion coupling and mass (right) recent limits on galactic axion coupling and mass. Figure taken from [26].	20
Figure 10	Plot showing calibration sources (Figure from [27]. The axis label subscript c denotes corrected variables with calibration for geometrical effects and electron lifetime (this calibration is discussed in further detail in Kr CALIBRATION Section)	23
Figure 11	Doke plot used to fit g_1 and g_2 for LUX Run03 (Figure from [27])	24
Figure 12	Large scale view of the experimental apparatus showing key parts.	30
Figure 13	Diagrams of two often used internal arrangements.	30
Figure 14	Pumping and instrumentation diagram of the test bed. Special symbols are labelled in the diagram, see key for other symbols. For readability, all gauges are not shown.	31
Figure 15	A picture of the CR-110 charge amplifier from the manufacturer's data sheet, shown with an equivalent circuit diagram.	32
Figure 16	A raw and shaped charge amp signal taken in -100C gaseous xenon, with the radon source plumbed in	32
Figure 17	(Left) original mounting of CR-110 charge amplifiers inside the experimental vessel. (Right) Mounting in the outer vacuum reduced heat load on the TPC.	33
Figure 18	Different lengths of BNC cable attached to a CR-110 test board.	34

Figure 19	(Left) Event showing charge amp with detector -100 C, 1.5 bar, gas only. (Middle) Effect of circulation pump on charge amp is to cause 500 Hz oscillation noise (-100 C, 1.5 bar, gas only). (Right) Same event as (middle), but zoomed-in time scale.	34
Figure 20	(Left) Periodic noise from the Glassman 20 kV negative polarity voltage supply. (Right) Partial breakdown in R60 cable as picked up by charge amplifiers.	35
Figure 21	A diagram showing components of the slow control.	36
Figure 22	A 12kV SHV weldable connector from vacuum supplier Kurt Lesker.	38
Figure 23	(left) The copper tape in this picture is sitting on top of a 1/2 -in swage connector. The swage connector captures a 1/2 in pipe, which has the 12 kV SHV feedthrough welded to the end. (right) 12 kV SHV weldable connector, inverted, clipped, and attached with a machined copper connector. The connector uses a screw to capture the SHV feed though, and the same screw to capture a stranded wire, visible in this picture, which is then fed through a hole drilled in the PTFE to connect to the wire grid frames. The wire was wrapped around the grid frame.	38
Figure 24	The same 12kV SHV feed through, now with a modified spring connection connecting the feed through to the grid frame. A close up of the cathode grid showing the spring connection is on the right	39
Figure 25	Oscilloscope showing baseline rate of single photons (left) compared to a high rate of single photons (right) caused by the high voltage feed through.	39
Figure 26	(Left) Full xenon breakdown as visible on the PMT trace. The large, saturated pulse is caused by the high intensity of light. This type of breakdown was often accompanied by an audible buzz, and a rise in current that would initiate a trip of the high voltage supply. (Right) a close up of the xenon-facing side of the feedthrough. Visible gaps where xenon gas is exposed to high fields are particularly problematic for breakdowns.	40

Figure 27	Top: (left) cathode connection side (right) SHV-20 connection side Bottom: (left) an example showing how the cable was attached to the stock SHV-20 feed though end (right) a custom cap fit over the connection, smoothing out triple points.	41
Figure 28	Effect of holding the feed through in place with PEEK zip ties was explored, effects were minimal.	41
Figure 29	The black line shows the aging observed in the course of normal operations. The red line shows breakdown tests of the SHV-20 feed though in gas, illustrating that the aging observed during operation was due to aging of the feed though.	42
Figure 30	First attempt at a custom feed through built out of Swagelock parts combined with basic materials like PTFE and stainless steel rods. The orientation shown (left) was later inverted due to concerns of temperature stress and pressure stress on the PTFE ferrules. The feedthrough as assembled (center) was functional, but higher voltage capability was desired. The effect of adding a grounding braid (right) was found to decrease the voltage capability instead of increasing it.	43
Figure 31	(top) Input to a COMSOL model simulating gaps between the grounding braid and dielectric of a high voltage feedthrough. (bottom) COMSOL output the model, showing that peak fields arise when gaps exist between dielectric and grounding braid.. Both images provided by high voltage engineer W. Waldron.	44
Figure 32	Top: (left) Close up showing the PTFE ferrules and notch. (right) Close up of the sealed top connection; epoxy was added to prevent leaks between the dielectric and conductor rod . Bottom: (left) Threaded U-bend cathode connector (right) Feed through assembled and installed.	45

Figure 33	Top: (left) Sealed top connection with liberal epoxy use. A male Bendix pin was soldered to the cable conductor. (middle) SHV connector with female Bendix to mate with feedthrough (right) Grounded safety housing with SHV connector. Bottom: (left) Ends of the feedthrough were held in the Teflon stack. (middle) Close up showing cable conductor, PTFE dielectric, and grounding sheath pulled back (right) Grounding scheme for feedthrough cables.	46
Figure 34	The ^{222}Rn decay scheme. The fast and slow chains are indicated.	48
Figure 35	Pathways to radon and radon daughter contamination.	49
Figure 36	Diagram of the test bed. For this study, the cathode is held at -6.0 kV, and the grid is held at -4.0 kV. $E_1^{\text{liq}} \approx 5.0 \text{ kV/cm}$, $E_1^{\text{gas}} \approx 10.0 \text{ kV/cm}$ $E_2 = 1.0 \text{ kV/cm}$. $E_3 = 2.7 \text{ kV/cm}$. The large gray regions represent the structural rings of PTFE. The line between the grid and anode represents the liquid xenon level. The xenon inlet pipes incoming gas directly into the liquid region, and the liquid outlet pulls from the level of the active region. A gas outlet (not pictured) also draws xenon gas into the circulation system to be purified.	51
Figure 37	An example a circulation path used for plate out is shown on the pumping and instrumentation diagram. During data-taking the radon source was bypassed. The typical liquid level is indicated on the diagram to show that the outlet drew from the liquid via a capillary, ensuring purification of the liquid xenon. A gas purge also purified the gas column in the detector. . .	52
Figure 38	The ^{220}Rn decay scheme. The fast and slow chains are indicated. Events in the plate out data sets are from the slow chain.	53
Figure 39	a) and (b) and (c) show the plateout conditions of datasets A, B, and C, respectively. The gray bands indicate time when data was being acquired. Dataset D (calibration) was taken following dataset A and consisted of a few hours. .	56

Figure 41	Monte Carlo study to find the maximum distance a ^{212}Bi beta (2.2 MeV) on the cathode could penetrate into the drift region. The projected range (red) is the relevant curve for this analysis; it shows a beta is not expected to travel more than 1.2mm from the cathode.	60
Figure 42	For datasets A and B: (left) Distribution of events in z . (right) The same events distributed in the S1-S2 plane, showing selection criteria for candidate ^{212}Bi alpha events in the bulk liquid xenon.	61
Figure 43	For datasets C and D: (left) Distribution of events in z . (right) The same events distributed in the S1-S2 plane, showing selection criteria for candidate ^{212}Bi alpha events in the bulk liquid xenon.	62

LIST OF TABLES

Table 1	Summary of plate out and data-taking conditions. Data sets A and B are taken after circulating radon gas and data set C, background, had no radon circulation. Data set D was taken following dataset A, and radon was circulated in a liquid xenon environment, purposefully introducing radon into the detector bulk to calibrate the detector.	54
Table 2	Calculations of fiducial volume. Liquid level is taken to be 14 ± 1 mm. Density of Liquid Xenon (LXe) near boiling point is 2.9 g/mL.	55
Table 3	Number of detected alpha particle events whose energy determination was consistent with ^{212}Bi decay to ^{208}Tl . Live times are quoted in Table 1	60
Table 4	Using observations from 3, proceed through solubility calculation.	65

ACRONYMS

SM	Standard Model
BSM	Beyond the Standard Model
SUSY	Supersymmetry
MSSM	Minimal Supersymmetric Model
cMSSM	Constrained MSSM
pMSSM	Phenomenological MSSM
LSP	Lightest Supersymmetric Particle
WIMP	Weakly Interacting Massive Particle
LIP	Lightly Ionizing Particle
LUX	Large Underground Xenon
LXe	Liquid Xenon
TPC	Time Projection Chamber
SURF	Sanford Underground Research Facility
ER	Electron Recoil
NR	Nuclear Recoil
HV	High Voltage
SHV	Safe High Voltage
SS	Stainless Steel
CF	Conflat
PMT	Photomultiplier Tube
QE	Quantum Efficiency
EEE	Electron Extraction Efficiency
PTFE	Polytetrafluoroethylene

PEEK Polyether ether ketone

RMS root mean square

CCS Collisional Cross Section

PAI Photo Absorption Ionization

FVP Fermi Virtual Photon

1

INTRODUCTION

I was dreamin' when I wrote this, forgive me if it goes astray.

— Prince, 1999, 1989

This Thesis is laid out like....

PART I

THEORETICAL CONTEXT AND EXPERIMENTAL STRATEGIES

This section describes the theoretical foundation for the analysis presented in [Part II](#). It includes an overview of the Standard Cosmology...

2

THEORETICAL BACKGROUND

2.1 A LITTLE HISTORY

Our understanding of the universe develops in a leap-frog of theory and observation, one catching up to and surpassing the other as technology improves, to be passed in turn by a new idea or new observation.

2.2 THE STANDARD COSMOLOGY

The standard cosmology is a parametrization of the Big-Bang cosmological model is also referred to as Λ CDM ("Lambda-CDM") and it accounts for the observed:

- cosmic microwave background (CMB)
- large scale structure of galaxies and clusters
- accelerating expansion of the universe
- abundances of hydrogen and helium

Since the CMB was discovered in 1965

2.3 EVIDENCE FOR DARK MATTER

2.3.1 GALAXIES AND CLUSTERS

2.3.2 COSMIC MICROWAVE BACKGROUND

2.4 DARK MATTER CANDIDATES MOTIVATED BY PARTICLE PHYSICS

2.4.1 WIMPS AND THE HIERARCHY PROBLEM

2.4.2 AXIONS AND THE STRONG CP PROBLEM

2.5 MOTIVATION FOR LIPS

2.6 EXPERIMENTAL STRATEGIES FOR DETECTING DARK MATTER

2.6.1 PRODUCTION

2.6.2 INDIRECT DETECTION

2.6.3 DIRECT DETECTION

3

PARTICLE DETECTION WITH LIQUID XENON

3.1 LIQUID XENON AS A DETECTOR MEDIUM

Liquid xenon detectors are powerful tools for rare event searches. In particular, the dual phase [LXe](#) Time Projection Chamber ([TPC](#)) has been very successful in accessing Weakly Interacting Massive Particle ([WIMP](#)) parameter space and currently holds the worlds most sensitive limits on [WIMPs](#). This section describes the properties of [LXe](#) and the basic principles of [TPCs](#) that have allowed this technology to play a large role in the hunt for dark matter.

3.1.1 PROPERTIES OF LIQUID XENON

Liquid xenon has many properties relevant to particle detection, particle identification, and also many properties related to the ease of detector operation:

- The density of [LXe](#) is 2.9 g/cm^3 at 170 K , much denser than other possible [TPC](#) target materials, such as liquid argon which has density 1.4 g/cm^3 at 87 K . The advantage in this two-fold: (1) the same volume contains more kg of Xe than Ar, so for two detectors of the same volume, one filled with Xe and the other with Ar, both running for one year, the Xe detector has more exposure; (2) xenon's high density effectively stops external radiation, producing an ultra-low-background volume in the center of the detector where rare-event searches can be performed (this region is called the “fiducial volume”).
- Xenon gas is easily liquefied with liquid nitrogen (77 K) or commercially available pulse tube refrigerators.
- Xenon has no long-lived radioisotopes that cause troublesome backgrounds. The one exception is the $2\nu\beta\beta$ decay of ^{136}Xe (natural abundance 8.875%) with measured half-life of $2.1 \times 10^{21} \text{ years}$. The long half-life and relatively low abundance together result in a very

low count rate, and the isotope can be used to search for neutrino-less double beta decay ($0\nu\beta\beta$).

- Xenon, as a noble element, is easily purified with a heated getter to rid electronegative impurities (e.g. O₂) that interfere with the ionization signal.
- The comparatively large mass of xenon allows it to be purified of other noble gasses via gas chromatography [1] and cryogenic distillation [2]. As other noble gasses cannot be removed via getter, this feature is extremely useful in removing the troublesome background of ⁸⁵Kr decay. ⁸⁵Kr decays via beta emission to stable ⁸⁵Rb with a half-life of 10.8 years and $Q_\beta = 687$ keV. The decay proceeds directly to the ⁸⁵Rb ground state with a branching ratio of 99.6%. Since no de-excitation of ⁸⁵Rb follows, this beta decay cannot be rejected as background by coincidence with a gamma, and relies purely on the ability to discriminate between WIMP-like Nuclear Recoil (NR) and beta- or gamma- produced Electron Recoil (ER). While ER/NR discrimination is one of the features of LXe TPCs (described in section 3.3.1.1), leakage of ER events into the NR signal region can occur and the best mitigation is to remove as much of the ⁸⁵Kr as possible. Single-phase LXe detectors, with no ER/NR discrimination, benefit greatly from the ability to remove ⁸⁵Kr.
- Particles interacting in LXe excite atoms and create electron ion-pairs, producing detectable quanta: scintillation photons and ionization electrons, respectively (described in section 3.1.2).
- Xenon produces scintillation light of wavelength $\lambda = 178$ nm (described in section 3.1.2). Xenon is transparent to this wavelength so it can propagate freely and be directly detected with current Photomultiplier Tube (PMT) technology, and doesn't require the use of e.g wavelength shifter.
- Ionization electrons produced in particle interactions can be drifted and extracted into a gaseous region via applied electric fields, where they undergo proportional scintillation. By this method, a single electron is amplified many-fold into detectable photons. This basic operating principle of dual-phase TPCs makes even a single ionization electron detectable.
- Xenon has high light and charge yields, and therefore a low threshold for producing detectable quanta. A useful quantity is the so-called ‘W-value’ of LXe: $W = 13.7 \pm 0.2$ eV [3]. The W-value, analogous to a work-function, is a measure of the average energy expen-

diture to produce one quanta (scintillation photon or an ionization electron) from liquid xenon.

- [LXe TPCs](#) are easily scalable: creating a large homogenous volume is straightforward. In contrast, solid state detectors, such as cryogenic Ge, are more difficult to scale up directly and require instead the production of multiple small modules ($O(10)$ cm) which each must be instrumented separately.

3.1.2 SCINTILLATION AND IONIZATION SIGNAL GENERATION

A particle can interact with a xenon atom through interaction with an orbiting electron, creating an [ER](#), or though an interaction with the xenon nucleus, where the nucleus is imparted with momentum and recoils, [NR](#). Some energy is lost to atomic motion (heat). The recoiling electron or nucleus loses energy via interaction with neighboring xenon atoms, creating more excited atoms and electron-ion pairs. The excited xenon atoms, Xe^* , combine with other atoms to form an excited dimer, or excitons, Xe_2^* . The excited dimer forms two states: a triplet and a singlet, which de-excite with the emission of a 178 nm photon. The lifetimes of the triplet and singlet are measured to be 24 ns and 3 ns, respectively [4]. Since the scintillation light is produced by the excimer, which has a different electronic structure than atomic xenon, the light is free to propagate through the detector and will not be absorbed by the atomic xenon. The Xe^+ ions of the electron-ion pairs combine with other Xe atoms to form dimers Xe_2^+ , and these dimers can combine with electrons (from the electron-ion pairs) to form excitons, Xe_2^* , which then decay and produce additional 178 nm scintillation photons. This process is called recombination. If no electric field is applied, all electron-ion pairs recombine to produce additional scintillation photons. If an external electric field is present, some electrons can be drifted away from the interaction site to be detected with other methods.

The sensitivity of liquid xenon detectors to low energy recoils depends on their ability to detect the 178 nm scintillation photons with high-efficiency. High Quantum Efficiency ([QE](#)) PMTs constructed with ultra-low radioactivity materials are the go-to instrument for this purpose. In addition to high-efficiency photon-detectors, liquid xenon detectors must also have high geometrical light collection efficiency to optimize sensitivity. Single-phase liquid xenon detectors, where no electric field is applied, maximize light-collection by with a spherical geometry, endeavoring to cover 4π steradians surrounding the [LXe](#). The XMASS detector uses spherical geometry to accomplish photocathode coverage of 62%, and two types of Hamamatsu PMTs (R10789-11 and R10789-11MOD) with [QE](#) of 28%, and

quote a signal collection efficiency of 20% [5], [6]. Dual-phase TPC detectors are lined with Polytetrafluoroethylene (PTFE) to take advantage of its extremely high (99%) reflectivity for 178 nm light in LXe [7]. The Large Underground Xenon (LUX) detector uses a cylindrical geometry, with all non-light-collecting surfaces lined with PTFE, and Hamamatsu R8778 PMTs (QE of 33%) only on the top and bottom of the detector (low photocathode coverage), to accomplish a light collection efficiency of 90% [8].

If the detector is a TPC the ionization electrons are drifted away from the interaction site to be detected. Single phase TPC employ thin wires to collect the ionization electrons. For example, the EXO-200 experiment is a single-phase liquid xenon TPC that uses crossed-wire planes to collect the ionization electrons and avalanche photodiodes to collect the scintillation photons [9]. LUX is a dual-phase xenon TPC, where ionization electrons produced in the large liquid region are drifted and extracted into gaseous xenon via applied electric fields, where they undergo proportional scintillation. The proportional scintillation light is the same 178 nm wavelength as scintillation in the liquid produced in the liquid, and it is similarly collected via high QE PMTs.

In addition to light-collection efficiency, the sensitivity of TPC xenon detectors also depends on their ability to collect signal from the ionization electrons. There are challenges in delivering High Voltage (HV) to liquid xenon in order to set up the electric field which drifts the ionization electrons (some of these challenges are explained in Chapter 6). Additionally, electronegative impurities such as oxygen (O_2) present in the detector attract and capture ionization electrons as they drift, eating away the ionization signal. These non-noble impurities are removed by constantly circulating the xenon through a heated zirconium getter and returning it to the detection volume. Purification through a getter must be done in gaseous phase, so liquid xenon removed from the detection volume is evaporated, passed through the getter via a circulation system, and re-condensed into the detection volume.

3.2 DUAL-PHASE XENON TIME PROJECTION CHAMBER

A particle interacting in a noble liquid or gas target deposits energy into scintillation and ionization channels (Section 3.1.2). The basic operating principle of TPCs is to drift the ionization electrons away from the interaction site and detect them at a later time than the scintillation signal is detected. A dual phase liquid xenon TPC is a type of TPC with a large liquid target volume and a small region of xenon vapor above the liquid volume,

instrumented with light sensors (typically PMTs). A particle interacting in the liquid target produces both scintillation photons and ionization electrons at the interaction site. The scintillation photons are promptly detected by the PMTs, this primary signal is called S1. The ionization electrons are drifted upward to the gas region by an applied electric field, and extracted across the liquid-gas boundary by a higher electric field, where they undergo proportional scintillation and produce a second signal detected by the PMTs, called S2. The field is supplied by a series of electrodes, composed of wire planes, grids, or chemically etched meshes, held at constant voltages. The bottom-most field-producing electrode is called the cathode, at the top of the liquid region is the gate or extraction electrode, followed O(1) cm by the anode. The liquid region is often referred to as the ‘drift region’ and region between the gate and anode is referred to as the ‘extraction region’. The drift region takes up by far more volume than the extraction region. The electrons are extracted from liquid to gas with some efficiency, called the Electron Extraction Efficiency (EEE). This efficiency plays an important role in the operation of dual-phase LXe TPCs, and is discussed further in **E-Train CHAPTER**.

The S2 in a dual-phase TPC plays two important roles: (i) internal amplification of the signal, whereby a few electrons are transformed into O(10) times as many photons (ii) (x, y) localization via PMT hit pattern. The time spacing of the S1 and S2 signals can be converted to depth (z) of the interaction, providing full (x, y, z)-reconstruction of the interaction position.

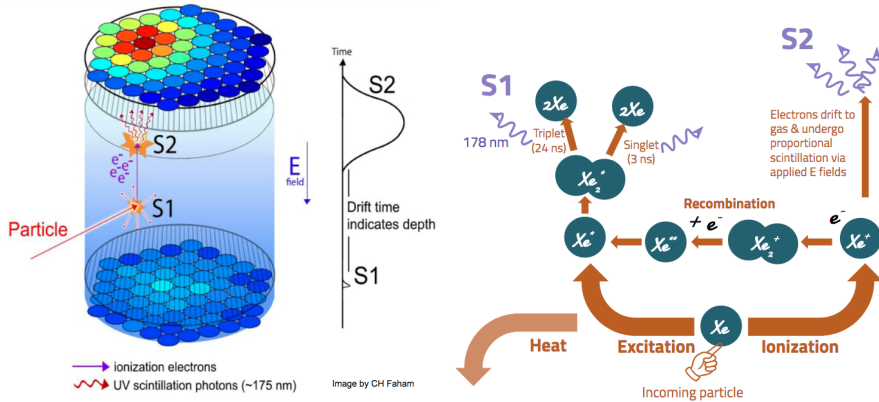


Figure 1: (left) Diagram of a dual-phase xenon time projection chamber. The time difference between S1 and S2 gives the depth (z) of the interaction, and (x, y) is reconstructed from the S2 signal. (right) Diagram summarizing the generation of the scintillation and ionization signal generation in dual-phase xenon time projection chambers.

3.2.1 ENERGY RECONSTRUCTION

Energy reconstruction in dual-phase xenon TPCs comes from the measurable quantities, S1 and S2, but begins with the number of excitons n_{ex} and electron-ions pairs n_i generated at the interaction site.

$$E = fW(n_{ex} + n_i) \quad (1)$$

where E is the deposited energy. W is the average energy needed to produce a single excited or ionized atom, $W = 13.7 \pm 0.2$ eV [4]. The quenching factor, f is 1 for electronic recoils but $f \neq 1$ for nuclear recoils. For now, take the case of electronic recoils and set $f = 1$. This equation can be rewritten:

$$E_{ER} = W\left(1 + \frac{n_{ex}}{n_i}\right)n_i \quad (2)$$

The ratio of excitons to ions is constant for electron recoils $n_{ex}/n_i = 0.2$ [10]. As discussed in Section 3.1.2, each exciton deexcites, emitting a 178 nm photon, some fraction r of the initial electron-ion pairs recombine and form additional excitons. The total number of prompt scintillation photons created by the interaction is then:

$$n_\gamma = \left(r + \frac{n_{ex}}{n_i}\right)n_i \quad (3)$$

And the total number of electrons created by interaction site (electrons escaping recombination) is:

$$n_e = (1 - r)n_i \quad (4)$$

Thus, the effect of recombination is to “trade-out” electrons for photons, but the total number of quanta is conserved (Figure 2 (left)). The amount of recombination depends on applied electric field, LXe density, and particle energy [10]. In the case of the 122 keV electron recoils in Figure 2 (right): at low fields, most of the electron-ion pairs recombine, which results in more scintillation photons. As the applied electric field increases, more electrons are pulled away from the interaction site resulting in fewer scintillation photons and more ionization electrons. These amounts of photons and electrons are referred to as the scintillation and ionization yields. The two quantities, n_γ and n_e relate directly to the observable S1 and S2 signals:

$$\begin{aligned} E_{ER} &= W(n_\gamma + n_e) \\ &= W\left(\frac{S1}{g_1} + \frac{S2}{g_2}\right) \end{aligned} \quad (5)$$

where E_{ER} reminds us that we are taking the case of electronic recoils and set $f = 1$ in Equation 5. S1 and S2 are in units of detected photons (phd), and g_1 and g_2 are detector gains in units of phd / quanta. g_1 is the detection efficiency for the prompt scintillation photons: it is a product of the average geometrical light collection efficiency and the average PMT QE. Typical values for g_1 are in the range of 0.01-0.02. g_2 is the analogous quantity for S2 proportional scintillation light: it is a product of the EEE and the average number of detected photons produced by one extracted electron. Typical values for g_2 are in the range 10-60.

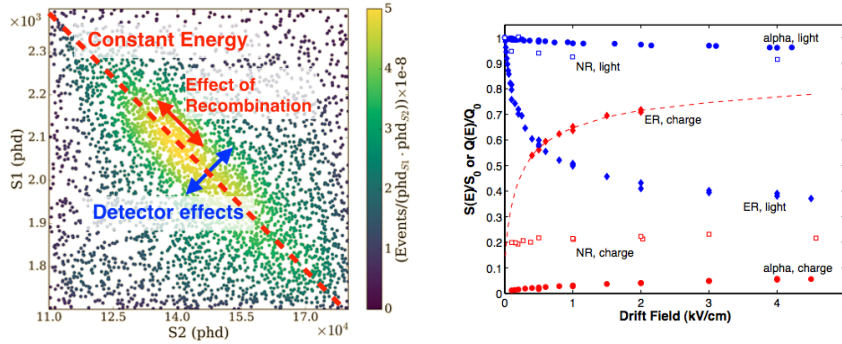


Figure 2: (left) Plot illustrating the effect of recombination and detector effects on a line source (127Xe), courtesy of E. Pease. (right) Field dependence of scintillation and ionization yield in LXe for 122 keV electron recoils (ER), 56.5 keV nuclear recoils (NR) and 5.5 MeV alphas, relative to the yield with no drift field from [11]

To properly reconstruct the energy of nuclear recoils, we must revisit the quenching factor f . Equation 5 then becomes:

$$\begin{aligned} E_{NR} &= fW(n_\gamma + n_e) \\ &= fW\left(\frac{S1}{g_1} + \frac{S2}{g_2}\right) \end{aligned} \quad (6)$$

This equation can be rewritten:

$$E_{NR} = fE_{ER} = \frac{E_{ER}}{\mathcal{L}} \quad (7)$$

where \mathcal{L} is Lindhard's factor. Lindhard's factor accounts for the fraction of energy lost to atomic motion (heat) in nuclear recoils [12]. An incoming particle interacts with a “patient zero” Xe atom, resulting in a nuclear recoil. The patient zero Xe atom interacts with surrounding atoms in a cascade to produce S1 and S2; it is the energy partitioning in this cascade that results in different energy scales for ER and NR. Lindhard shows

that the energy partitioned in nuclear interactions and electron interactions from a recoiling xenon nucleus is:

$$\mathcal{L} = \frac{kg(\epsilon)}{1 + kg(\epsilon)} \quad (8)$$

where $k = 0.133Z^{2/3}A^{-1/2}$ is a proportionality constant that relates electronic stopping power and the velocity of the recoiling xenon atom, and $\epsilon = 11.5(E_{NR}/\text{keV})Z^{-7/3}$. Lindhard's calculation yields $k = 0.166$, which is the commonly accepted value. Measurements of nuclear recoils in LXe are used to fit for k . Several experiments were compared by Sorensen and Dahl to determine that nuclear recoil energy is well described by $0.110 < k < 0.166$ [13]. Results from LUX yielded $k = 0.1735 \pm 0.0060$ [14].

If it is not known *a priori* whether an interaction is a nuclear recoil or electron recoil, the ‘electron equivalent’ energy is given in units keV_{ee} . If it is known that the recoil is a nuclear recoil, Lindhard’s factor is applied and the units are given keV_{nr} . Lindhard’s factor allows us to combine nuclear recoils and electronic recoils on one scale by labelling contours of constant reconstructed energy with both keV_{ee} and keV_{nr} (example in Figure 3).

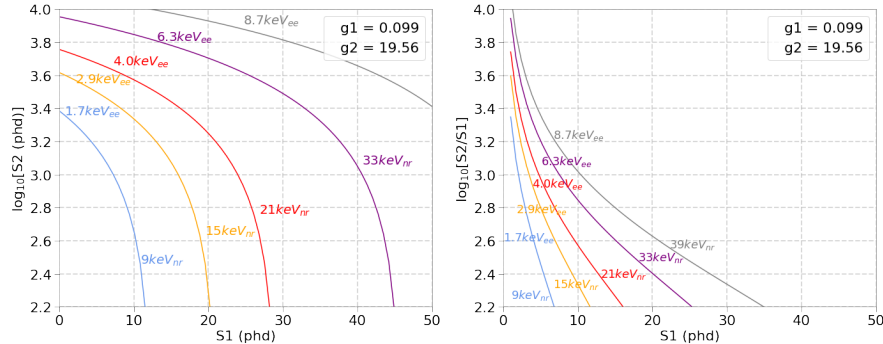


Figure 3: Plots showing combined energy contours in two common sets of axis units, for an example set of g_1 and g_2 .

3.3 DUAL-PHASE XENON TPCS FOR DARK MATTER DETECTION

Dual phase Xe TPCs have been at the forefront of the hunt for dark matter in the last several decades. As described above, the xenon medium and detector technology make excellent low-background, rare-event searches

with high signal yields. Dual phase Xe TPCs also provide a few enhancements to WIMP dark matter searches, but other dark matter or rare event searches are also possible with the same detector.

3.3.1 WIMP SEARCHES WITH LXE TPCS

Dual-phase LXe TPCs are optimized for WIMP searches. They have been very successful in reaching large areas of WIMP parameter space.

3.3.1.1 ER, NR DISCRIMINATION

One of the most powerful features of LXe TPCs, which has made the technology especially useful in the hunt for WIMP dark matter, is the ability to discriminate between electron recoils and nuclear recoils. WIMP interactions are expected to be nuclear recoils, but most natural radioactivity (β, γ) are electron recoils. The amount of recombination for equal energy ER and NR is different, so for events with the same reconstructed energy $E(\text{keV}_{ee})$, the ratio of S_2/S_1 is characteristically different. A useful discrimination space is $\log_{10}(S_2/S_1)$ vs S_1 , as the distributions of $\log_{10}(S_2/S_1)$ for ER and NR events are Gaussian. Different calibration sources are used to develop a population of events known to be ER and a population of events known to be NR, these calibration sources reveal what is known as the ER and NR bands (Figure 4).

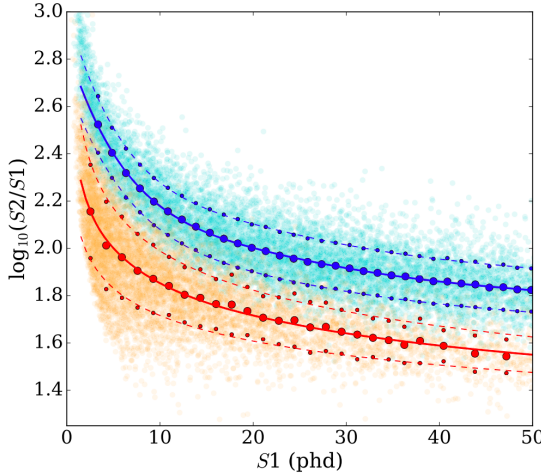


Figure 4: Plot showing ER and NR bands from LUX. Solid lines are the ER and NR Gaussian means μ , dotted lines are $\mu \pm 1\sigma$. Figure from [10]

In the course of a WIMP search, the experimentalists are tasked with keeping a stable detector operating for months or years. In this time, the detector will see events of natural radioactivity and perhaps WIMPs. The

natural radioactivity appears in the **ER** band (location of bands is known from calibration), and nuclear recoil events appear in the **NR** band. Due to band overlap, only events appearing below the **NR** mean are considered **WIMP** candidates. This restriction cuts signal acceptance to 50%, but allows dual-phase **TPCs** to reject background electronic recoils at $\gtrsim 99\%$. The background acceptance rate is known as **ER** leakage. It is the fraction of events appearing below the **NR** mean from the **ER** calibration source. For a background rejection rate of 99.99%, the **ER** leakage is 0.01%, this number determines the sensitivity of the detector.

3.3.1.2 WIMP RATES AND CROSS SECTION

The choice of direct detection for **WIMP** searches was touched on [??](#). Here, we go through the specifics of **WIMP** rates and their cross section in **LXe**, showing that the **LXe TPC** technology gets an enhancement that makes it especially suited for **WIMP** searches.

WIMPs scattering in the **TPC** produce measurable nuclear recoils. The shape of this nuclear recoil spectrum determines eventually the number of **WIMP** events observed, and it depends on both **WIMP** properties and detector properties. The energy imparted to nucleus depends on **WIMP** mass M_χ and velocity distribution, as well as the mass of the target nucleus M_T and a nuclear form factor F that governs how effectively energy is transferred to the nucleus. Assuming a uniform, spherical dark matter halo, estimates for the local density of dark matter ρ_χ can be made from astrophysical observations. The velocity distribution $f(v)$ is assumed to be isotropic and Maxwellian, with a cut-off at the escape velocity v_{esc} of the Milky Way. If we account for the velocity of the Earth through the galactic plane v_E , the velocity distribution is shifted: $f(v) = f(v, v_E)$. Following Lewin and Smith [\[15\]](#), we can write the local number density:

$$\begin{aligned} dn &= \frac{n_0}{k} f(v, v_E) d^3v \\ &= \frac{n_0}{k} \exp\left(-\frac{(v + v_E)^2}{v_0^2}\right) d^3v \end{aligned} \tag{9}$$

Where $n_0 = p_\chi/M_\chi$ is the average local number density of dark matter particles, $v_0 \approx 220 \text{ km/s}$ [\[?\]](#) is the mean of the dark matter velocity distribution, and k is a normalization constant such that $\int_0^{v_{esc}} n_0 dv \equiv n_0$. If the escape velocity is infinite, the normalization integral is easily evaluated:

$$k = \int_0^{2\pi} \int_{-1}^{1i} d(\cos\theta) \int_0^\infty f(v, v_E) v^2 dv = (\pi v_0^2)^{3/2} \equiv k_0 \tag{10}$$

v_{esc} is not infinite ($v_{esc} \approx 544 \text{ km/s}$ [16]), and so the normalization integral evaluates to:

$$k = k_0 \left[\operatorname{erf}\left(\frac{v_{esc}}{v_0}\right) - \frac{2}{\pi^{1/2}} \frac{v_{esc}}{v_0} \exp(-v_{esc}^2/v_0^2) \right] \equiv k_1 \quad (11)$$

Although this is a more complicated expression, it should be noted the difference between k_0 and k_1 is less than 0.5%. We now have a full picture of the local number density of dark matter, and we focus on the scattering rate in the detector. If we let σ be the scattering cross-section per nucleus (the details of σ are discussed later), the event rate per unit mass detector with target mass M_T is:

$$dR = \frac{1}{M_T} \sigma v dn \quad (12)$$

The experimentalist is concerned with the observable recoil energy spectrum produced by such a dark matter rate. A **WIMP** of mass M_χ and initial energy $E_\chi = \frac{1}{2} M_\chi v^2$ scattering at angle θ (in the center-of-mass frame) will impart a recoil energy E_R to a target nucleus of M_T

$$E_R = r E_\chi \frac{1 - \cos\theta}{2} \quad (13)$$

Where r is the kinematic factor:

$$r = \frac{4M_\chi M_T}{(M_\chi + M_T)^2} \quad (14)$$

Note that the kinematic factor indicates that recoil energies are greatest for $M_\chi \approx M_T$. SUSY models favor **WIMP** masses in the range 100GeV-1000GeV (Figure 6), which makes xenon ($M_{Xe} \approx 123 \text{ GeV}$) an excellent target. **WIMP** scatters are assumed to be isotropic, so recoil energies are distributed uniformly in the range $0 < E_R < rE_\chi$ (i.e. Equation 13 for $0 < \cos\theta < 1$). We can put this together with Equation 12 to arrive at an differential rate per recoil energy in the detector – i.e. the observable recoil spectrum for **WIMP**-nucleus scattering. Note that equation Equation 12 is in terms of the **WIMP** velocity v and Equation 13 is in terms of **WIMP** energy $E_\chi = \frac{1}{2} M_\chi v^2$, so a change of variables is required. After the variable change, we can write:

$$\frac{dR}{dE_R} = \frac{\rho_\chi}{M_\chi} \frac{\sigma}{k} \left(\frac{M_T + M_\chi}{M_T M_\chi} \right)^2 \int_{v_{min}}^{v_{max}} \frac{1}{v} f(v, v_E) d^3v \quad (15)$$

Until now, we have left off discussion of the [WIMP](#)-nucleus cross section σ . Equation 15, as it stands is the [WIMP](#) spectrum in the limit of billiard-ball coherent scattering. In reality, nucleus has structure which must be accounted for, which is accomplished with a nuclear form factor $F = F(q)$. In addition, the cross-section is split into spin-independent (σ_{SI}) and spin-dependent (σ_{SD}) components:

$$\sigma = \sigma_{SI}F_{SI}^2(q) + \sigma_{SD}F_{SD}^2(q) \quad (16)$$

The nuclear form factor, $F(q)_{SI,SD}$, decreases the cross section at higher momentum transfer. The two coherent terms σ_{SI} and σ_{SD} are parametrized as follows:

$$\begin{aligned} \sigma_{SI} &= \frac{4\mu^2}{\pi}[(A-Z)f_n + Zf_p]^2 \\ &\approx \frac{4\mu^2 A^2}{\pi}f_n^2 \end{aligned} \quad (17)$$

Where μ is the usual reduced mass, and the second line takes into account that for Supersymmetry ([SUSY](#)) [WIMP](#) models, the couplings to neutrons and protons are approximately equal ($f_n \approx f_p$).

$$\sigma_{SD} = \frac{32G_F\mu^2}{\pi} \frac{J+1}{J} [\langle s_n \rangle a_n + \langle s_p \rangle a_p]^2 \quad (18)$$

Where G_F is the Fermi constant, J is the total nuclear spin of the target, and $\langle s_{n,p} \rangle$ and $a_{n,p}$ represent values for neutron and proton spins and couplings, respectively. It should be noted that σ_{SI} scales as A^2 , which indicates a cross-section enhancement for larger targets. σ_{SD} lacks the A^2 scaling, and is smaller σ_{SI} . This indicates that recoil-rates are dominated by spin-dependent interactions. The two cases are treated separately, with collaborations releasing both spin-independent and spin-dependent [WIMP](#) limits. in liquid xenon detectors, the odd-numbered nuclei ^{129}Xe and ^{131}Xe contribute to the spin-dependent rate. The enhancements for the [WIMP](#) recoil rate in Xe are illustrated in Figure 5

3.3.2 OTHER DARK MATTER SEARCHES WITH LXE TPCS

The available [SUSY](#) parameter space has dwindled greatly in the last few decades, due in large part to the success of this detector technology. Coupled with no observation of [SUSY](#) at the **LHC!** (**LHC!**), experimentalists are beginning to look to other models and parameter spaces for dark matter. New technologies are being developed and refined for new dark matter

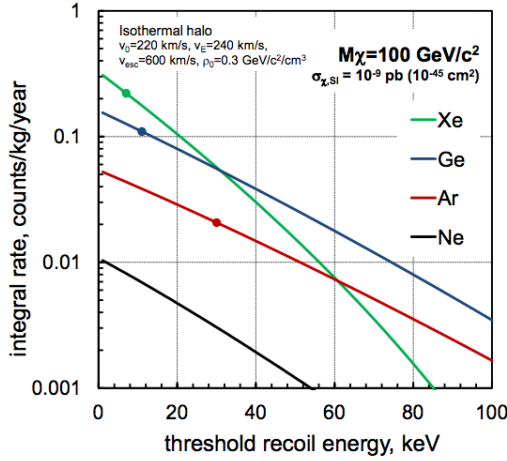


Figure 5: Plot showing spin-independent WIMP rates in common detector target materials, dots indicate typical thresholds for the targets. Xenon gains in favored SUSY parameter space ($M_\chi \gtrsim 100$ GeV) due to a kinematic enhancement ($M_\chi \sim M_{Xe}$) and a cross-section enhancement ($\sigma_{SI} \propto A^2$). Figure from [17]

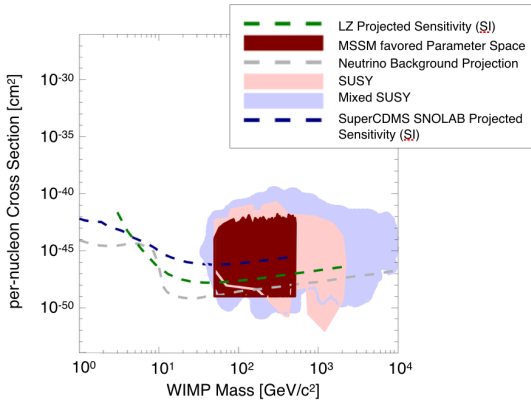


Figure 6: Projected limits of next-generation dark matter detectors and areas where SUSY models predict the presence of WIMPs. Although Xe (LZ, green dashed) performs better for WIMP parameter space, Ge and Si (SuperCDMS, blue dashed) can access other light dark matter parameter space below 10 GeV. The plot was generated by <http://dmtools.brown.edu/>

candidates, but already existing, well-understood detector technologies such as dual-phase TPCs can also be employed in the search for non-WIMP dark matter.

In their first WIMP search results, the Xenon10 collaboration imposed an analysis threshold of 4.5 keV_{nr} [18]. The first LUX results set an analysis threshold of 4.3 keV_{nr} (with $2 < S1(\text{phd}) < 30$ and $S2(\text{phd}) > 200$; $S2(\text{electrons}) \gtrsim 8$) [19]. The first Xenon100 results set an analysis threshold of 8.7 keV_{nr} ($4 < S1(\text{phd}) < 20$ and $S2(\text{phd}) > 300$; $S2(\text{electrons}) \gtrsim 10$) [20]. Such thresholds are common practice, and are set by the light-collection efficiency of the detector; the detection threshold is much lower. Dual-phase TPCs are sensitive to events which produce a single electron, due to the internal amplification of the S2 signal; the reason for setting analysis thresholds is to ensure the presence of an S1 in the event. Without both S1 and S2 in the event, the full (x,y,z) position cannot be reconstructed, and so a fiducial cut cannot be applied. Sorensen showed that the Xenon10 S2 pulse width carries a mild z-dependence [21], and so larger detectors with a long drift time may gain reliable z-position reconstruction via S2 pulse width [22]. Improvements in analysis techniques such as this allow dual-phase xenon TPCs to reach lower WIMP masses, and even other dark matter models.

In 2011 the Xenon10 collaboration presented a search for low-mass (5 - 20 GeV) dark matter [23]. The detector conditions were distinct from the Xenon10 WIMP search in [18]: the secondary scintillation gain was about 12% higher, and the S2-sensitive trigger threshold was set at the level of a single electron. With this, the collaboration carried out a standard WIMP analysis (i.e one based on the procedure presented in 3.3.1.2), with a lowered S2 analysis threshold of 4 electrons (1.4 keV_{nr}). Why they did not proceed down to the detection threshold of 1 electron is very interesting; and is discussed further in Chapter ???. Since Xenon10 is a small detector, they were not able to take advantage of S2-width z-correlations, but they employed a radial fiducial cut and other analysis techniques to produce the result in Figure 7.

A few years later, Essig et al. used the information reported in [23] and other Xenon10 publications to produce the first direct detection limits of sub-Gev dark matter [24]. The detection threshold for WIMPs in LXe decreases sharply for $M_{WIMP} \lesssim 10 \text{ GeV}$; however, this detection threshold is based on the assumption that the dark matter is interacting only with the xenon nucleus. If sub-GeV dark matter scatters with atomic *electrons*, as opposed to nuclei, then it can produce observable signals of a few electrons; in LXe TPCs the S1 signal is lost due to light collection, and the few electron signals are observable as S2s. The approach in the paper is to follow approximately the same procedure as in Section 3.3.1.2, with a few but significant substitutions. The E_R in Equation 13 must now ac-

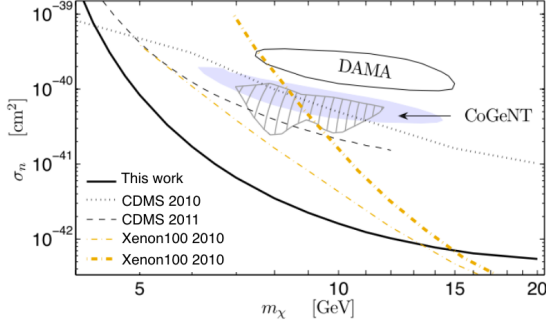


Figure 7: Xenon 10 low-mass WIMP limit extended the range of the standard WIMP result.

count for the binding energy of the electron, and take a different form to refer to the recoil of the electron and not the nucleus. The cross section of interest is now σ_e , the sum over all of the differential ionization cross sections for electrons in the (n, l) shell. For a dark photon with mass $O(\text{MeV-GeV})$ coupled to the visible sector via kinetic mixing (a very generic class of standard model extensions discussed in Chapter ??, Essig et al. set the exclusion limit in the $m_{DM} - \sigma_e$ plane in Figure 8 (left). If there is some momentum-transfer enhancement due to e.g. scattering through an electric-dipole moment, $\sigma_e \rightarrow \sigma_e F_{DM}(q) \equiv \bar{\sigma}_e$. Essig set exclusion limits for such dark matter candidates in Figure 8 (right).

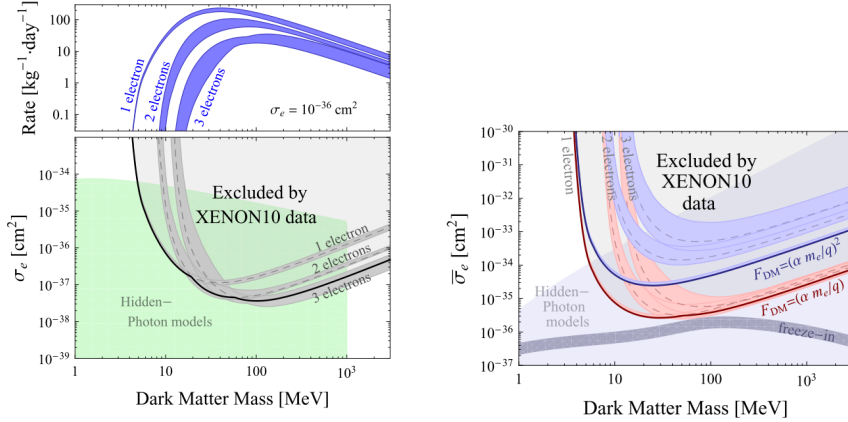


Figure 8: (left) Top: Expected 1,2,3-electron signal rates for Sub-GeV DM with $\sigma_e = 10^{-36} \text{ cm}^2$ and Bottom: exclusion limit set with Xenon10 few-electron signals. (right) Exclusion limits for dark matter scattering through an electric-dipole moment (red) and through a very light ($\ll \text{keV}$) mediator (blue)

In addition to the dark sector, dual-phase TPCs can search for other dark matter signals with scattering on electrons. Annual modulation searches

(in ER or NR) can provide clues to dark matter. Such searches take advantage of the fact that v_E varies with the rotation of the earth around the sun, reaching a maximum in June and minimum in December. The modulation in v_E leads to a modulation in the recoil rate observed in the detector. Searches for dark matter-induced rate modulations can offer a generic approach to identify dark matter interactions, complementary to the model-driven dark matter searches. The LUX experiment did such a search, looking at ER modulations in an energy range of interest ($2\text{-}6 \text{ keV}_{ee}$). This energy range was chosen to overlap with the DAMA/LIBRA Collaboration’s long-standing and controversial claim of dark matter modulation on a target of NaI(Tl), which appears strongest around a recoil energy of 3 keV_{ee} . LUX found no significant indication of rate modulation [25]. If future large dual-phase TPCs like XenonNT and LZ observe a NR WIMP signal, the additional positive identification of a modulation signal of the NR signal would be a smoking-gun for WIMP discovery.

Another dark matter candidate that could produce an electron recoil signal in xenon is the axion (or more generally, axion-like-particles). For searches such as these, a signal model is produced from the spectrum of axions from different sources, such as galactic axions or solar axions. The resulting signal model is an ER spectrum accounts for finite detector energy resolution and threshold. The signal model spectrum is compared to the observed ER spectrum in the appropriate energy ranges, resulting in a confidence statement mass of the axion m_A and the axio-electric coupling g_{Ae} . The results of searches for solar axion and galactic axion signals are shown in Figure 9.

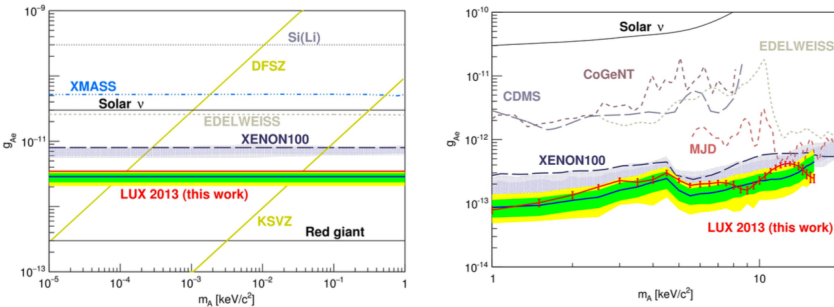


Figure 9: (left) Recent limits on solar axion coupling and mass (right) recent limits on galactic axion coupling and mass. Figure taken from [26].

Finally, a model-independent search for Lightly Ionizing Particle (LIP)s is possible in dual-phase xenon TPC. As discussed in Chapter ??, LIPs appear in dark sector models with a masses dark photon, where another dark sector particle χ couples to the standard model electron via kinetic mixing of the dark photon and standard model photon. LIPs deposit en-

ergies that can be described with particles of effective fractional charge. Chapter ?? describes the signal model and analysis method to search for LIPs in [LUX](#).

PART II

BIG SCIENCE

This section describes research done with the LUX Detector.

4

THE LUX DETECTOR

4.1 DETECTOR COMPONENTS

4.1.1 CRYOSTAT

4.1.2 PMTS

4.1.3 WATER TANK

4.1.4 TRIGGER AND DATA ACQUISITION

4.2 CALIBRATIONS

4.2.1 ENERGY

Two or more calibration line sources of different energies are used to fit for g_1 and g_2 . The [LUX](#) experiment uses a suite of sources to calibrate the detector, the sources used to calibrate the energy response of the detector for Run03 are shown in [10](#) along with pictoral explanation of the effect of recombination on energy reconstruction.

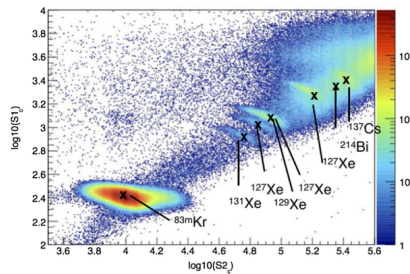


Figure 10: Plot showing calibration sources (Figure from [\[27\]](#). The axis label subscript c denotes corrected variables with calibration for geometrical effects and electron lifetime (this calibration is discussed in further detail in **Kr CALIBRATION Section**)

The average S1 and S2 of each calibration source is normalized to the true energy:

$$(S1, S2) \rightarrow \left(\frac{\langle S1 \rangle}{E}, \frac{\langle S2 \rangle}{E} \right) \quad (19)$$

and a line $y = mx + b$ is fit to the transformed variables, where the slope is $m = -g_1/g_2$ and the y-intercept is $b = g_1/W$.

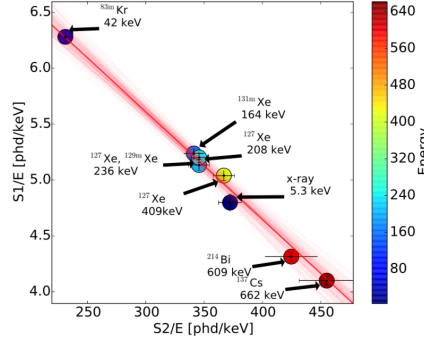


Figure 11: Doke plot used to fit g_1 and g_2 for LUX Run03 (Figure from [27])

From the fit in Figure 11, the the LUX gains were measured to be $g_1 = 0.117 \pm 0.003$ phd/photon and $g_2 = 12.1 \pm 0.8$ phd/electron, with an EEE of $49\% \pm 3\%$ [27].

4.2.2 TRITIUM

4.2.3 DD

4.2.4 KR

5

LIGHTLY IONIZING PARTICLE SEARCH

*And all this science I don't understand,
It's just my job five days a week*

— Elton John *Rocket Man*, 1972

5.1 MODELING LIP INTERACTION

5.1.1 COLLISION CROSS SECTION

A LIP interacting in the LXe volume loses energy via interaction with electrons. To model LIPs in LUX, the expression of interest is the collision cross section Collisional Cross Section (CCS). The differential CCS describes the energy lost to electrons in a single collision for incident energy of the LIP. For particles with charge ze and mass M heavier than the electron mass, m_e (“heavy” particles), the Rutherford cross section is a familiar differential CCS [28]:

$$\frac{d\sigma_R}{dE} = \frac{2\pi r_e^2 c^2 z^2}{\beta^2} \frac{1 - \beta^2 E/T_{max}}{E^2} \quad (20)$$

where r_e is the classical electron radius, E is the energy loss of incoming particle, $\beta = v/c$ of the incoming particle, and T_{max} is the maximum energy transfer possible in a single collision:

$$T_{max} = \frac{2m_2 c^2 \beta^2 \gamma^2}{1 + 2\gamma m_2/M + (m_e/M)^2} \quad (21)$$

Often the expression $T_{max} 2m_e c^2 \beta^2 \gamma^2$ for $2\gamma m_2/M \ll 1$ is used implicitly, or is referred to as the “low energy approximation” in older texts. The Rutherford cross section is a good starting point, but it describes the “hard interaction” or head-on, billiard-ball type collision of a particle interacting with free electrons. Real electrons are bound in atoms, and an incident particle can undergo “soft interactions”, in which virtual photons are exchanged. When the virtual photon matches the energy of electron

orbitals of the target material, there are resonances in the **CCS**. The energy transfer, E , must also be finite in real atoms, where the dielectric properties modify the electromagnetic field of a moving charged particle and limit the growth of the cross section. This real-world behavior is described by a correction factor $B(E)$, also sometimes called an “inelastic form factor” [28]:

$$\frac{d\sigma_{CCS}}{dE} = \frac{d\sigma_R}{dE} B(E) \quad (22)$$

Various attempts, spanning a better half of the last century, have been made to take into account the real-world behavior of electrons bound in matter. Some of these can be found in [cite 18,27, 41-43 papers from Bichsel]. More well-known contributions are those of Bethe and Fano. In 1930, Bethe derived a cross section doubly differential in energy loss and momentum transfer using the first Born approximation for scattering on free atoms [29]. In 1963, Fano extended the method to describe atoms in solids [30]. Combining their two methods yields the Bethe-Fano cross-section, which has undergone much study and by our current understanding has been verified to be close to reality [31]. There is another method, called the Photo Absorption Ionization (**PAI**) model, that is easier to calculate than the Bethe-Fano cross section, and approximates the Bethe-Fano calculation very closely. This thesis uses the **PAI** model as a base, building the full signal model for **LIPs** interacting in the **LUX** detector.

5.1.2 PHOTO ABSORPTION IONIZATION MODEL FOR CHARGE PARTICLE ENERGY LOSS

The **PAI** model is also sometimes known as the Fermi Virtual Photon (**FVP**) or WeisÖcker-Williams approximation. A full description of the **PAI** model is described in detail in [32]. The complex dielectric constant $\epsilon = \epsilon_1 + i\epsilon_2$ can be thought of as encoding all the information about a medium. The real part ϵ_1 describes the polarization of the material and imaginary part ϵ_2 describes the absorptive properties. Typically both ϵ_1 and ϵ_2 are thought of as functions of ω , or incident photon energy. So $\epsilon(\omega) = \epsilon_1(\omega) + i\epsilon_2(\omega)$. This description is limited to free photons, but we desire to describe inelastic collisions as well. So $\epsilon(k, \omega)$, a generalized dielectric constant, is introduced to describe momentum transfer k to atomic electrons. The generalized dielectric constant $\epsilon(k, \omega)$ can be related to atomic matrix elements, and if desired, calculated completely and tediously. However, the **PAI** model allows us to avoid these tedious calculations by making specific approximations, which, when taken together, define the **PAI** model itself.

In particular, the PAI model approximates $\epsilon_2(k, \omega)$ by noting that typically, the momentum k transferred to an electron is much less than the energy transfer ω .

5.1.3 STRAGGLING

5.1.4 ENERGY RESOLUTION IN LUX

5.1.5 POSITION RESOLUTION IN LUX

5.2 LIP SEARCH

5.2.1 LUX RUN03 CONDITIONS

5.3 LIP SEARCH ANALYSIS

5.3.1 ENERGY CONSISTENCY

5.3.2 TRACK LINEARITY CRITERIA

5.3.3 BACKGROUND REJECTION

5.3.4 MUONS

5.3.5 GAMMAS

5.3.6 ELECTRON TRAINS?

5.4 RESULT: VERTICAL FLUX LIMIT

PART III

LITTLE SCIENCE

This section describes research with a small test bed at Lawrence Berkeley National Lab.

6

RESEARCH AND DEVELOPMENT FOR FUTURE LXE TPCS

All systems go, are you sure?

— Peter Schilling *Major Tom*, 1969

A small test bed was built at Lawrence Berkeley National Laboratory to study various detector effects facing large [LXE TPCs](#). The test bed was built and instrumented over the course of about two years, from 2015 through 2016. This chapter describes some of the details of that instrumentation.

6.1 TEST BED APPARATUS OVERVIEW

The experimental apparatus consisted of an inner vessel, a vacuum outer vessel, and a xenon circulation system. The inner vessel was a Stainless Steel ([SS](#)) canister, topped with a 2.75 in Conflat-adaptable tower that allowed space for instrumentation cabling and [HV](#) feedthroughs. The inner vessel was offset below a 7.09 in ISO K flange, which held the (removable) vacuum outer vessel in place. Several Mini-CF ports were welded to the ISO K flange for instrumentation cabling. A large-scale overview is shown in Figure 12.

The inner vessel contained the [TPC](#). A PTFE housing cylinder fastened a PMT in place. Above the PTFE housing, a series of interlocking PTFE rings held strung wire grids and a segmented anode in place. During data taking, the entire PMT and housing were immersed in [LXe](#). The liquid level was chosen depending on the experiment at hand, approximated by the S2 width. In some cases, the TPC was “overfilled” by allowing the liquid level to rise above the anode. The segmented anode was instrumented with charge amplifiers for direct charge readout. When the [TPC](#) was overfilled, the charge amplifiers detected the ionization electrons directly from the liquid. During typical dual phase [TPC](#) operation, the charge amplifiers provided a secondary measurement of the ionization electrons in addition to S2. Two typical arrangements of the inner vessel are shown in Figure 13.

6.1 TEST BED APPARATUS OVERVIEW

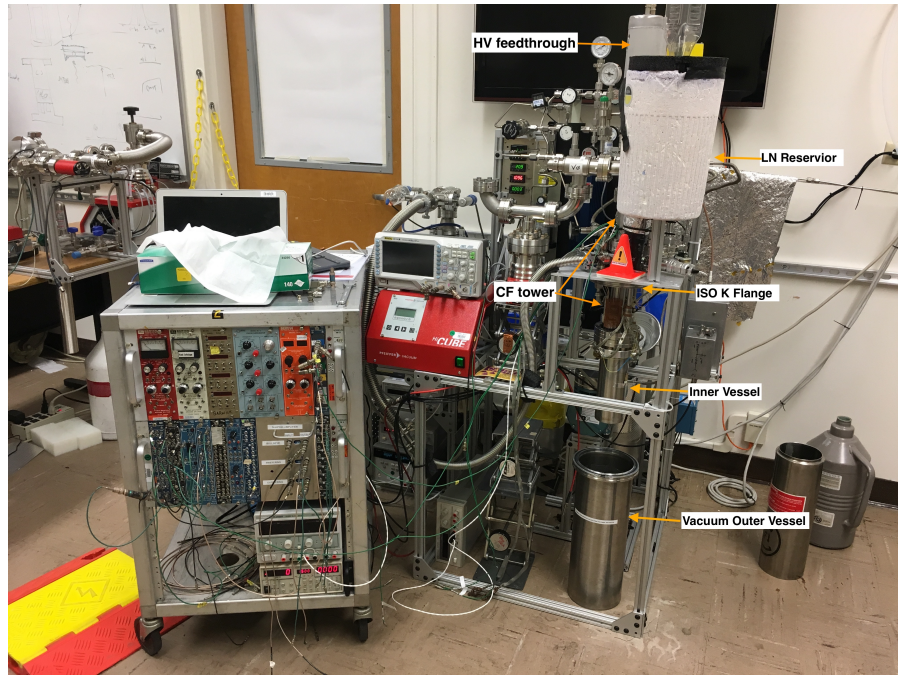


Figure 12: Large scale view of the experimental apparatus showing key parts.

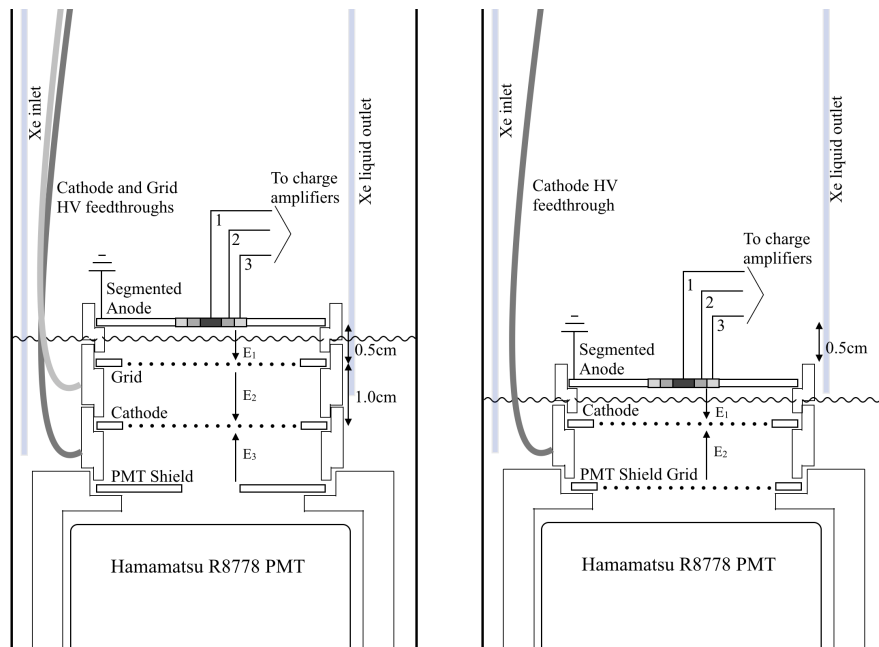


Figure 13: Diagrams of two often used internal arrangements.

6.2 CIRCULATION SYSTEM

The xenon circulation system is shown in Figure 14. A stainless steel capillary extending into the liquid drew xenon from the inner vessel during operation to be purified. Purified xenon that was returned to the vessel was directed into the liquid via a PTFE tube so it could condense quickly. A gas purge was added to the Conflat (CF) tower above the inner vessel to continually renew the gas column.

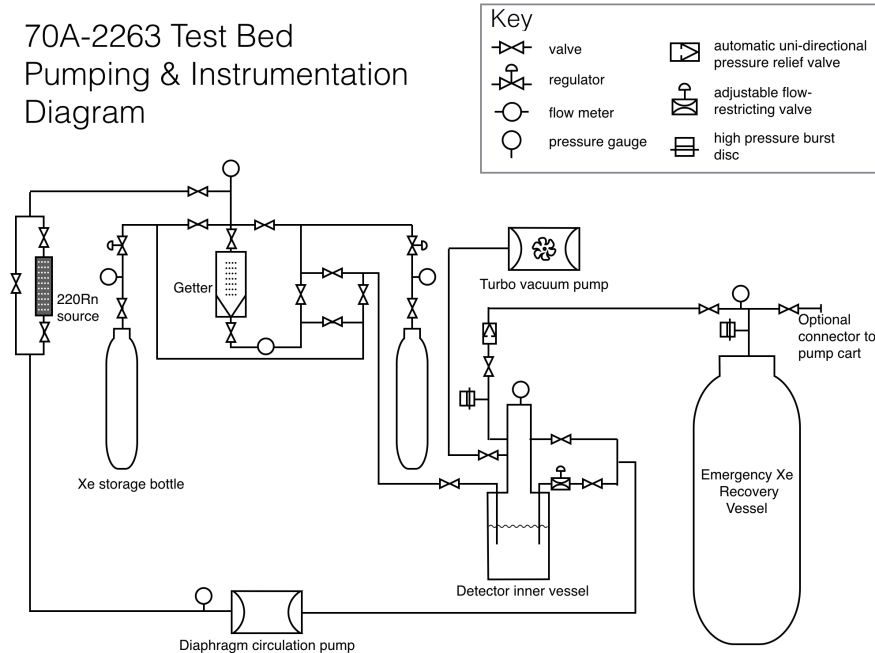


Figure 14: Pumping and instrumentation diagram of the test bed. Special symbols are labelled in the diagram, see key for other symbols. For readability, all gauges are not shown.

6.3 CHARGE AMPLIFIERS

The segmented anode was instrumented with three CR-110 charge amplifiers from Cremat (Figure 15). The raw charge amplifier signals were each fed into a CR-160-R7 shaper evaluation board, also from Cremat. The evaluation board houses two more modules: one CR-200-X shaping amplifier and one CR-110 baseline restorer. The CR-200-X shaping amplifier is an X- μ s gaussian shaping amplifier; it was determined that 1 μ s was most appropriate for the test bed signals.

The shaper evaluation board produced gaussian pulses from raw charge signals as shown in Figure 16.

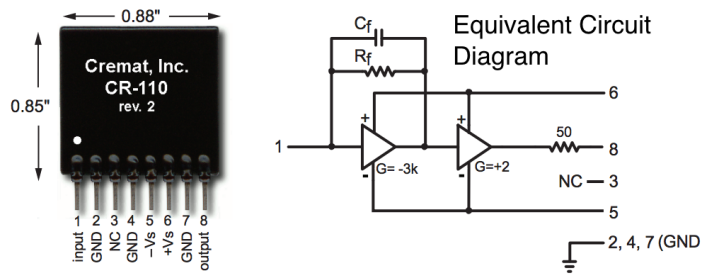


Figure 15: A picture of the CR-110 charge amplifier from the manufacturer's data sheet, shown with an equivalent circuit diagram.

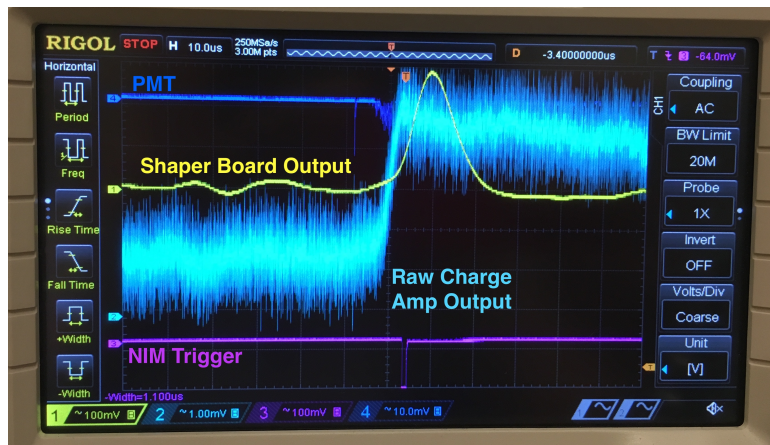


Figure 16: A raw and shaped charge amp signal taken in -100C gaseous xenon, with the radon source plumbed in

The charge amplifiers were originally placed inside the experimental vessel, mounted directly on the segmented anode. The functionality in [LXe](#) conditions didn't deviate from manufacturer's specifications, however it was found that the CR-110 units generated enough heat to create a perpetual gas layer under the anode. In general this is not an issue, but for the purpose of the intended absolute electron extraction efficiency measurement, overfilling the [TPC](#) and using the charge amplifiers as a direct read-out of electrons in the liquid was required. The charge amplifiers were moved to the outer vessel space, surrounded by a small Faraday cage made of copper mesh. See Figure 17 for the charge amplifier mounting configurations.

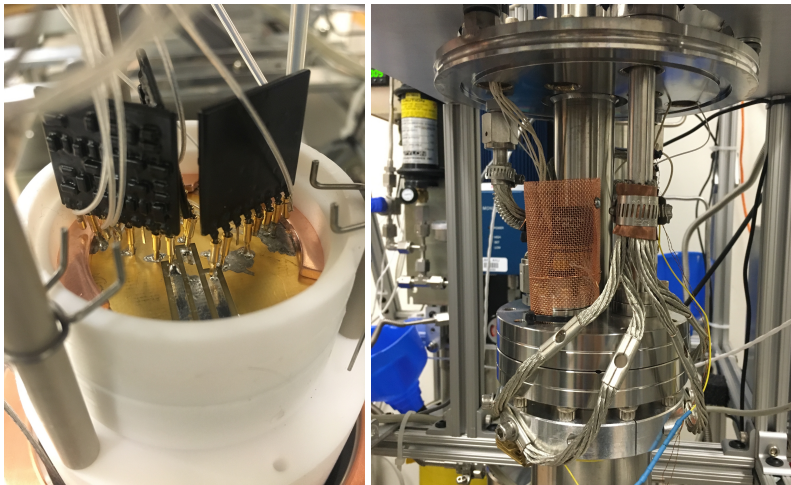


Figure 17: (Left) original mounting of CR-110 charge amplifiers inside the experimental vessel. (Right) Mounting in the outer vacuum reduced heat load on the TPC.

6.3.1 CHARGE AMPLIFIER NOISE BEHAVIOR

Charge amplifiers have baseline RMS noise proportional to the attached capacitance. Figure 18 shows the RMS noise of a CR-110 unit attached to different lengths of BNC cable. The longer the cable, the higher the RMS noise. [TPCs](#) are essentially capacitors, and when filled with [LXe](#) have a higher capacitance than when the detector is at vacuum. The capacitance of large [LXe TPCs](#) like [LUX](#) prohibit the use of charge amplifiers for direct readout of the S2 electrons because the RMS noise would swamp the signal.

Charge amplifiers also respond to acoustics. Tapping a finger near a charge amplifier will show as a baseline-jumping response on an oscilloscope. This additional source of noise makes [LXe TPCs](#) challenging places

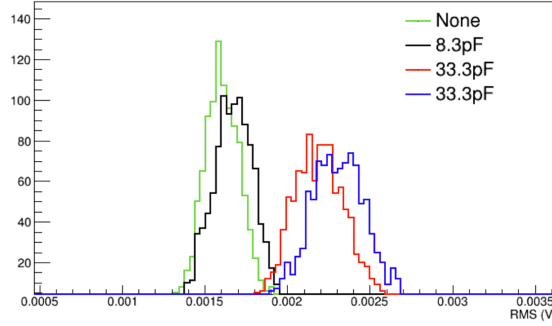


Figure 18: Different lengths of BNC cable attached to a CR-110 test board.

to use charge amplifiers for signal readout because any bubbles in the [LXe](#) create micro-acoustic signals which the charge amplifiers pick up. By design, dual phase [LXe TPCs](#) are operated near the xenon liquid-gas boundary so the formation and dissipation of gas bubbles in the liquid is likely. Additional sources of acoustic noise like circulation of xenon into the experimental vessel also produce visible responses in charge amplifiers. The difference in micro-acoustic noise environment is illustrated in Figure 19.

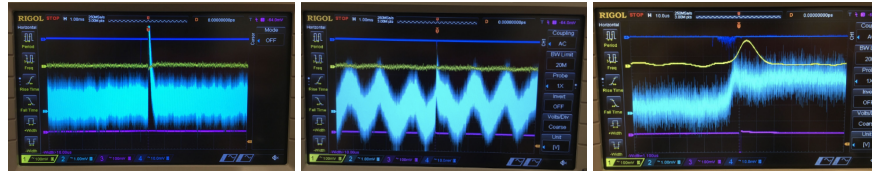


Figure 19: (Left) Event showing charge amp with detector -100 C, 1.5 bar, gas only. (Middle) Effect of circulation pump on charge amp is to cause 500 Hz oscillation noise (-100 C, 1.5 bar, gas only). (Right) Same event as (middle), but zoomed-in time scale.

As [TPCs](#) are large capacitors, any transients coupling to the “TPC capacitor” may be picked up by the charge amplifiers. In particular, instabilities in the [HV](#) chain induce a current in the “TPC capacitor” that is picked up by the charge amps. Instabilities in [HV](#) can come from many places. It was observed that for the characteristic capacitance and impedance of the the test bed, partial breakdowns in a length of R60 cabling caused a disruption in the functionality of the charge amplifiers. It was also found that a standard laboratory [HV](#) supply, a Glassman 20 kV negative polarity unit, created pick-up in the charge amplifiers (see Figure 20).



Figure 20: (Left) Periodic noise from the Glassman 20 kV negative polarity voltage supply. (Right) Partial breakdown in R60 cable as picked up by charge amplifiers.

6.4 PMT

The test bed was instrumented with an R8778 PMT, the same PMTs used in LUX. Both LUX and LZ PMT bases were used. The radon daughters study presented in Chapter 7 exclusively used the LUX PMT base, the electron trains studies first used the LUX base, and later used the LZ base. The LZ base was favored for its larger capacitors. Various shaping amplifiers were used when digitizing the PMT over the course of these studies because the 8 ns sampling interval of the data acquisition was subject to aliasing the fast-rising alpha S1 signals.

6.5 SLOW CONTROL

The slow control for the test bed consists of a few monitoring variables such as temperature and pressure, and a voltage supply that turns on heaters. The inner experimental vessel was instrumented with two platinum RTDs to monitor temperature and a capacitance manometer to monitor pressure. A flow meter in the circulation line determined the flow rate of xenon as it passed through the getter and returned to the inner vessel. These four variables are read using Omega i-series digital panel meters to provide a real-time display; two points of calibration are provided to the digital panel meters to translate voltage to human-readable pressure, temperature, etc. In addition, two $25\ \Omega$ resistors are mounted, in parallel, on the cold-head. Supplying voltage to these resistors raises the temperature of the cold-head and decreases the cooling power delivered by the liquid nitrogen bath; the voltage supplied to the heaters was also recorded, but not shown with digital panel meters. The voltages for the monitoring variables and the heater voltages were fed into a USB Device from Measurement Computing, which interfaces with a computer. A slow control script on a lab computer recorded the monitoring variables and heater

voltages. The script also determined if power should be supplied to the heaters and if text message and e-mail alarms should be sent for a variable out of expected range. A basic schematic of the slow control is shown in Figure 21.

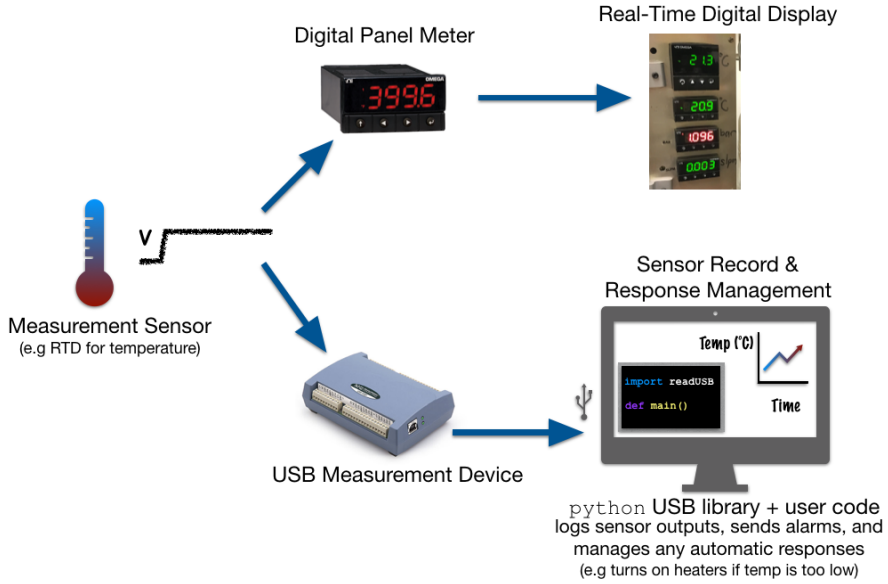


Figure 21: A diagram showing components of the slow control.

6.6 DATA ACQUISITION

Data were acquired with a Picoscope 5000a, a USB-compatible “oscilloscope.” The picoscope python library was used to write voltage records of PMT and charge signals to ROOT files, which were opened later for reprocessing into reduced quantities such as pulse area or pulse height. The picoscope was run as a 14 bit ADC with 125 MHz (8 ns) sampling. For special cases, when only one channel was desired, it was possible to increase the sampling rate to 500 MHZ (2 ns).

6.7 HIGH VOLTAGE FEEDTHROUGH DESIGN

A significant amount of time was spent developing and testing HV feedthroughs for the test bed. This section describes a few of the feedthroughs that were unsuccessful, leading to the final design, which is capable of delivering -11kV to the cathode with no observable breakdown or other effects. Extensive detail of the tests and procedures are not provided. Instead, the

following vignettes are intended as an overview to be useful to a student tasked with designing a HV feedthrough.

6.7.1 IMPLEMENTING SHV FEED THROUGHS FROM VACUUM SUPPLIERS

The first attempts at building feedthroughs were to use off-the-shelf products from typical vacuum supply vendors such as MDC and Kurt Lesker. Vacuum HV feedthroughs are intended to for use from air to vacuum, not air to LXe; we were attempting to operate them outside of their intended usage parameters. Additionally, by combining ceramic and metal (typically aluminum, stainless steel, nickel, copper) they are especially prone to breakdown at the meeting of these different materials, known colloquially as “triple points”. When there are interfaces between materials with different permittivities (dielectric constants), the electric fields are distorted. Electric field is “pushed” out of the higher dielectric material into the lower dielectric material. This creates a field enhancement where peak fields can be much higher than average fields in the system. The field enhancement from triple points where there is an interface between a conductor and two dielectrics (e.g conductor, ceramic insulator, and gaseous Xe) is a common source of breakdown along insulator surfaces. Good design practices, namely choices of geometry, reduce the field enhancements in these regions. With commercial feedthroughs, the geometry choice is set and may not be sufficient for the task.

Note that ceramic feedthroughs are not appropriate for low background experiments due to their high radioactivity, but for test beds, where low radioactivity is not a priority, they may be used.

The first few feed throughs used a 12kV Safe High Voltage (SHV) weldable feed though as shown in Figure 22. If used as operation is intended, the side indicated by A is used on the vacuum-side and B connects to the voltage supply. Instead, we trimmed the long B side and attached a copper, screw-port connector to make the 90 degree connection from vertical feed through to horizontal grid. This was done to avoid placing a conducting surface at high voltage (the tip of side A) in gaseous xenon, thereby increasing the risk of breakdown to the walls of the detector. The feed through’s vertical placement is designed such that the copper connector is fully submersed in LXe (Figure ??).

Feed throughs were tested by performing a cool down, ramping the HV supply slowly, and watching an oscilloscope for a higher than baseline photon rate (Figure 25) or a full xenon breakdown (Figure 26). The effect of raising the voltage on the HV supply at a specific rate was also tested, and it was determined that the extremely slow and steady rate of a computer program was not necessarily superior to the imperfect method

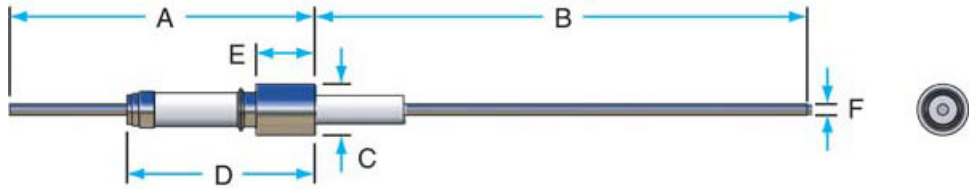


Figure 22: A 12kV SHV weldable connector from vacuum supplier Kurt Lesker.



Figure 23: (left) The copper tape in this picture is sitting on top of a 1/2 -in swage connector. The swage connector captures a 1/2 in pipe, which has the 12 kV SHV feedthrough welded to the end. (right) 12 kV SHV weldable connector, inverted, clipped, and attached with a machined copper connector. The connector uses a screw to capture the SHV feed though, and the same screw to capture a stranded wire, visible in this picture, which is then fed through a hole drilled in the PTFE to connect to the wire grid frames. The wire was wrapped around the grid frame.

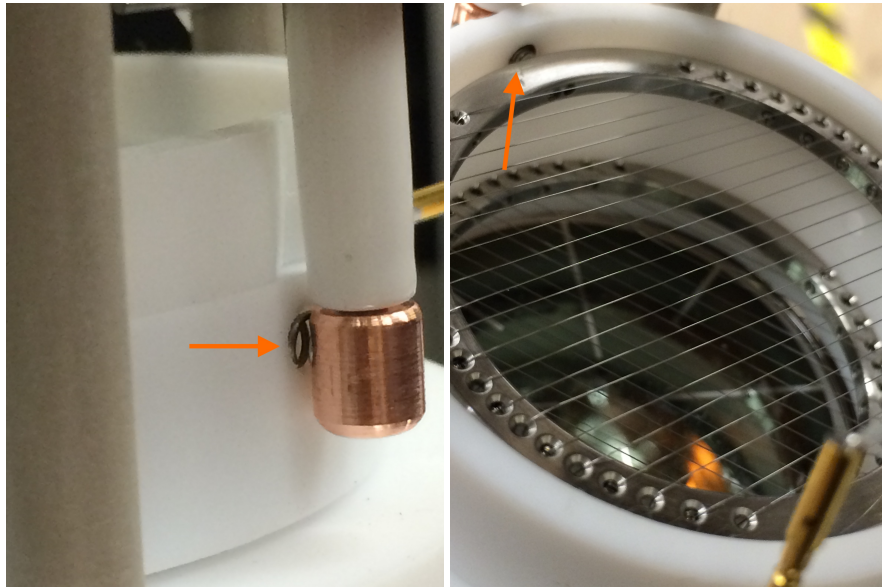


Figure 24: The same 12kV SHV feed through, now with a modified spring connection connecting the feed through to the grid frame. A close up of the cathode grid showing the spring connection is on the **right**

of the human experimenter – the construction of the feedthrough, itself, outweighed any gains from computer-supervised voltage ramping.

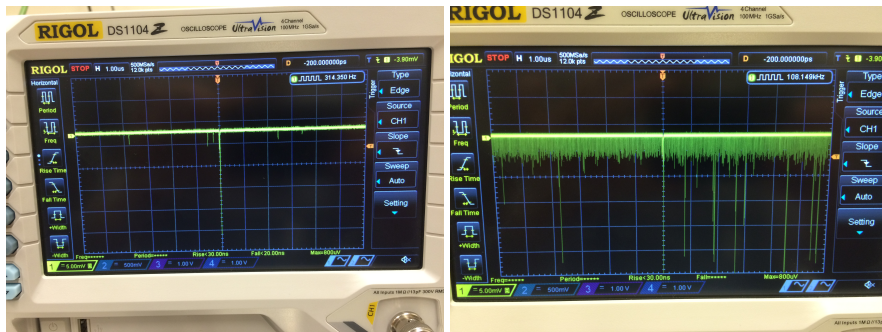


Figure 25: Oscilloscope showing baseline rate of single photons (left) compared to a high rate of single photons (right) caused by the high voltage feed through.

Iterations of the 12 kV SHV feed though were not able to reach and sustain more than about 7 kV for extended periods of time like those that would be required for data acquisition.

We also tried a stock 20 kV SHV feed through with a custom end cap designed by HV engineer Will Waldron, meant to smooth out typical triple point issues. This feed through was mounted on a CF flange far from the active region. A length of cable was stripped of grounding sheath for its

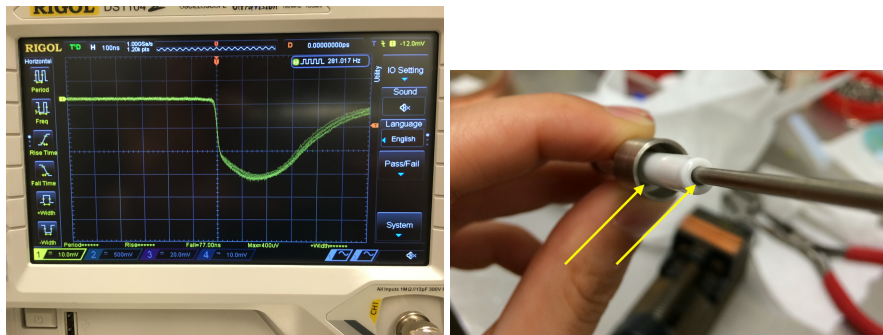


Figure 26: (Left) Full xenon breakdown as visible on the PMT trace. The large, saturated pulse is caused by the high intensity of light. This type of breakdown was often accompanied by an audible buzz, and a rise in current that would initiate a trip of the high voltage supply. (Right) a close up of the xenon-facing side of the feedthrough. Visible gaps where xenon gas is exposed to high fields are particularly problematic for breakdowns.

entire length. A small section on one end was stripped of dielectric, this end was tied to the SHV feed though with copper wire, and the custom end cap was placed over this. The side of the cable making the connection to the cathode grid was drilled out for a short length on the bottom, leaving only a tube of dielectric with no conductor. A threaded rod was inserted into the cable, such that the rod made contact with the conductor. The cathode grid frame was screwed onto the threaded rod. The SHV-20 feed though is summarized in pictures in Figure 27, and was found to hold sufficient voltage (10 kV) for extended periods of time. However, it was found that the voltage capability of this feed though decreased over time; this is discussed in the next section.

6.7.1.1 FEEDTHROUGH AGING

It was noticed during subsequent operation that the SHV-20 feed through was subject to some sort of aging process (black line in Figure 29). A month of use resulted in noticeably lower voltage capabilities. The issue could have been any point along the entire voltage chain: feed through - custom cap - connection to cable - cable - connection to grid - grid. Tests focusing on different parts of the voltage chain didn't reveal any weak points. Instead, it was found that the SHV-20 feed though, itself, was subject to aging (red line in Figure 29).

Feedthrough aging can be the result of arcing and discharges which cause local heating and carbonization of an insulator surface. Once there is a carbon path, the insulator is considered "tracked" and then holds a much lower voltage than before. Sophisticated HV systems keep peak cur-

6.7 HIGH VOLTAGE FEEDTHROUGH DESIGN

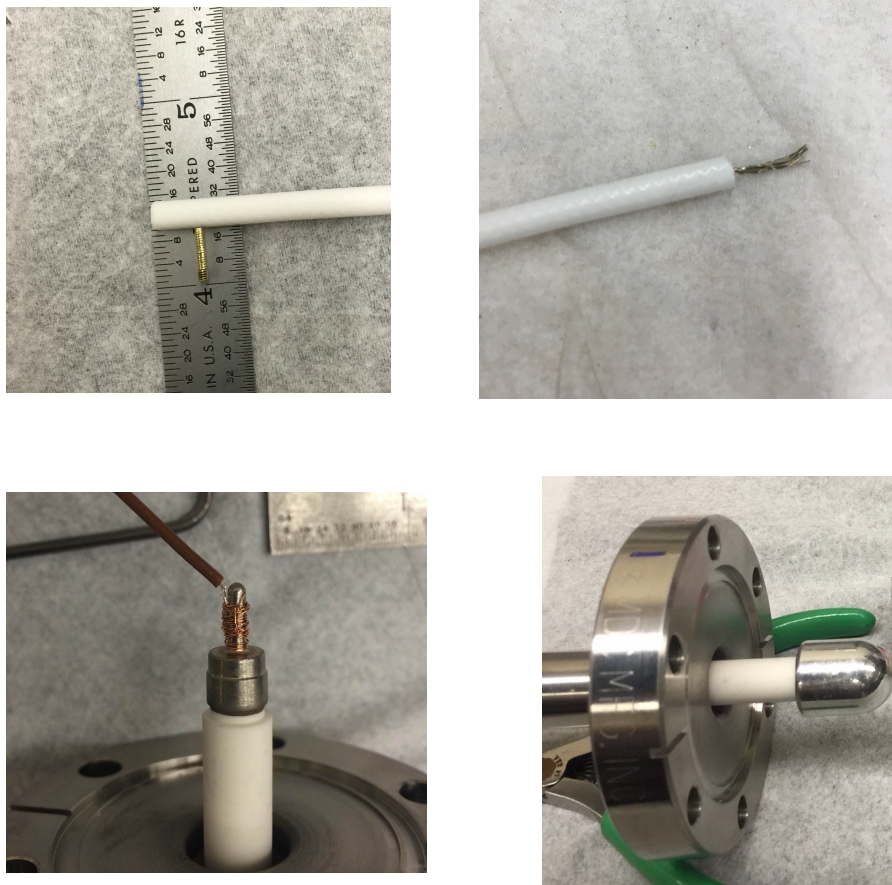


Figure 27: Top: (left) cathode connection side (right) SHV-20 connection side
Bottom: (left) an example showing how the cable was attached to the stock SHV-20 feed though end (right) a custom cap fit over the connection, smoothing out triple points.



Figure 28: Effect of holding the feed through in place with PEEK zip ties was explored, effects were minimal.

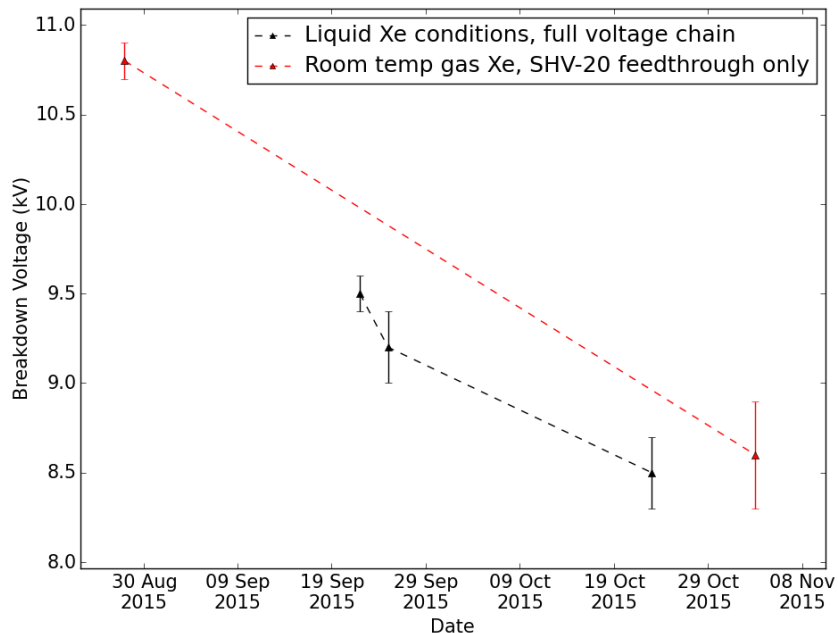


Figure 29: The black line shows the aging observed in the course of normal operations. The red line shows breakdown tests of the SHV-20 feed through in gas, illustrating that the aging observed during operation was due to aging of the feed though.

rents and fault energies to a minimum using series resistors. In this way, a breakdown event does not degrade system performance in the future. In addition to carbon tracks, there can also be insulator degradation from exposure to UV if there is ionization in the region. Xenon ionization is in the UV region of the spectrum, and so any ionization near a feed through insulator may degrade the feed through performance. In the case of this particular feed though, the high field which caused the breakdowns or ionization was likely a result of poor triple-point geometry.

6.7.2 CUSTOM FEEDTHROUGHS

To achieve better voltage performance, we moved away from typical, stock feedthroughs composed of ceramic and metal. Figure 30 shows a feed through made with a Swagelock reducing union. This blue and white PTFE piece connects 1/4 in SS pipe to an 1/8 in PTFE tube, which then houses a SS rod. The rod is screwed onto a connector, which holds a wire to connect to the grid. This feed through had stable voltage performance, but could not achieve sustained voltages higher than about 9 kV. A woven SS shield was added to the feed though to reach higher voltages (Figure 30 (left)) but this actually decreased the voltage performance to a maximum of about 5 kV.

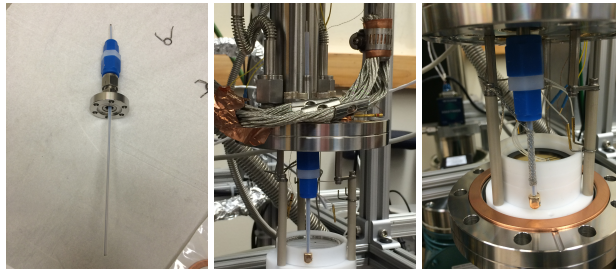


Figure 30: First attempt at a custom feed through built out of Swagelock parts combined with basic materials like PTFE and stainless steel rods. The orientation shown (left) was later inverted due to concerns of temperature stress and pressure stress on the PTFE ferrules. The feedthrough as assembled (center) was functional, but higher voltage capability was desired. The effect of adding a grounding braid (right) was found to decrease the voltage capability instead of increasing it.

There are two issues with the approach of adding a grounding braid in this method: (1) the braid is not tight to the dielectric, which introduces peak fields between the dielectric and the braid (Figure 31)(2) at the braid termination, a small effective radius creates an enhanced radial field through the dielectric and an enhanced field along the cable dielectric facing the high voltage. Peak fields can occur in unexpected places, greatly

decreasing the voltage capability of a feedthrough that seems, naively, robust. The breakdown field of xenon gas depends on a variety of factors such as temperature (i.e density), purity, electrode shape, etc. Peak fields arising in gas regions in or around HV feedthroughs are sources of unwanted light and in the worst case complete breakdown and eventual degradation of the feedthrough.

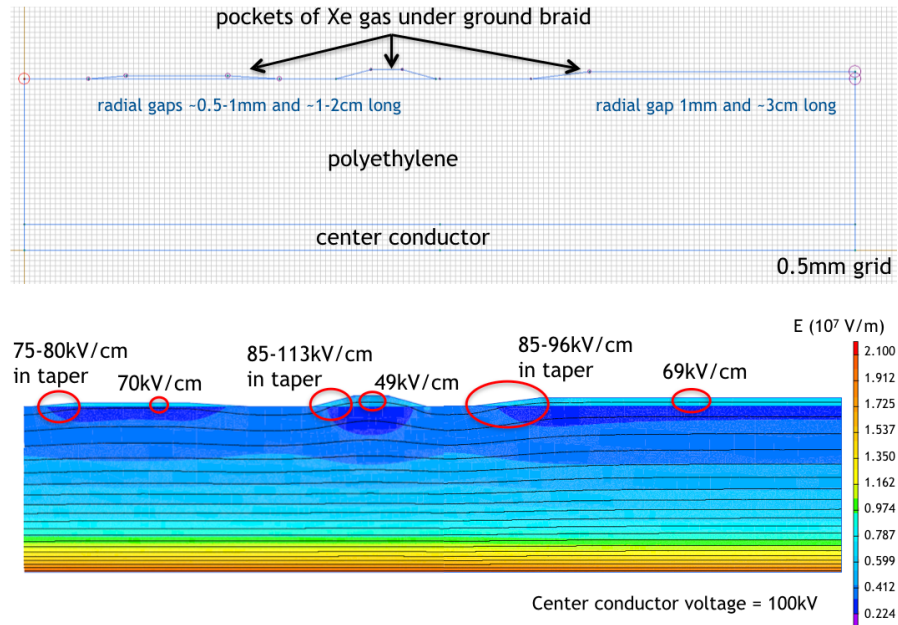


Figure 31: (top) Input to a COMSOL model simulating gaps between the grounding braid and dielectric of a high voltage feedthrough. (bottom) COMSOL output the model, showing that peak fields arise when gaps exist between dielectric and grounding braid.. Both images provided by high voltage engineer W. Waldron.

Due to the poor performance of custom feedthrough, and concerns about the cold connection, a feedthrough was built out of a SS rod with PTFE dielectric and no shield braid (Figure 32) that enters the inner vessel from the top of tall CF tower, where the connection is warm. The end is a copper rod bent into a U-shape which connects to the SS conduction rod via a pin, and the other end, which is threaded, screws into to the cathode grid frame. The bare copper section is only exposed under the liquid level, elsewhere the PTFE dielectric helps contain the electric field and prevent breakdown to the inner vessel wall. This feedthrough had good voltage performance, and there was no sign of aging. It was decided, however, that the charge amplifiers were more susceptible to detecting transients from an unshielded feedthrough, so another feedthrough with shielding was constructed (Figure 33). This feedthrough has an outer PTFE sheath to keep the shielding tight against the inner dielectric. This

6.7 HIGH VOLTAGE FEEDTHROUGH DESIGN

final feedthrough design was extremely successful, and has been in use for 2 years at the time of writing this thesis.

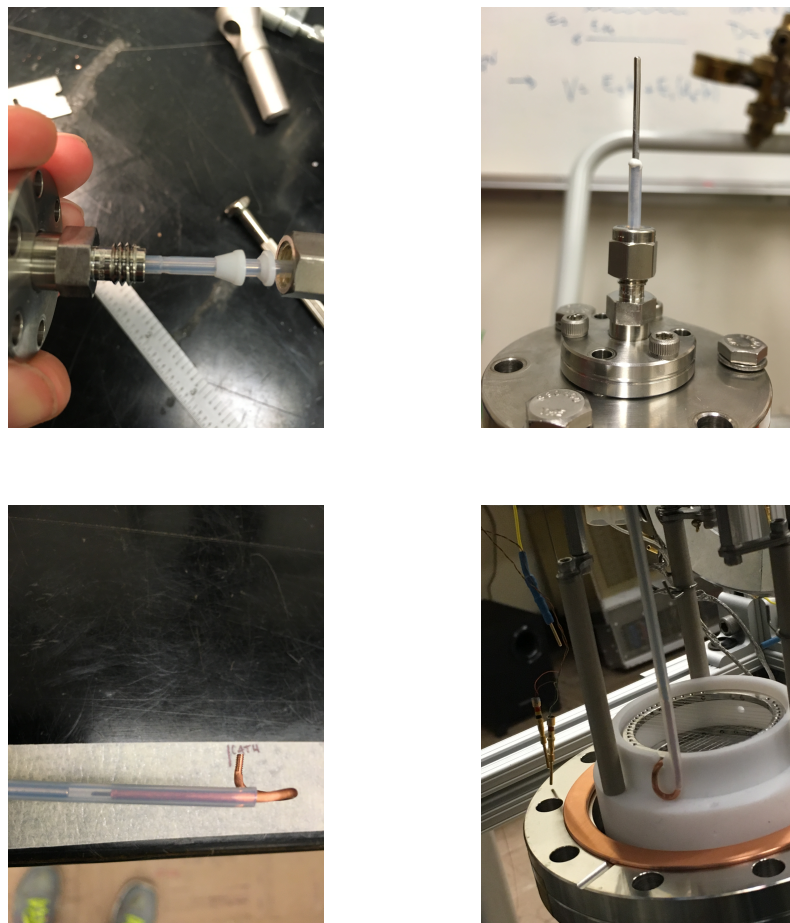


Figure 32: Top: (left) Close up showing the PTFE ferrules and notch. (right) Close up of the sealed top connection; epoxy was added to prevent leaks between the dielectric and conductor rod . Bottom: (left) Threaded U-bend cathode connector (right) Feed through assembled and installed.



Figure 33: Top: (left) Sealed top connection with liberal epoxy use. A male Bendix pin was soldered to the cable conductor. (middle) SHV connector with female Bendix to mate with feedthrough (right) Grounded safety housing with SHV connector. Bottom: (left) Ends of the feedthrough were held in the Teflon stack. (middle) Close up showing cable conductor, PTFE dielectric, and grounding sheath pulled back (right) Grounding scheme for feedthrough cables.

7

SOLUBILITY OF RADON DAUGHTERS IN LIQUID XENON

Rare-event searches are very sensitive to backgrounds from radioactivity in and on detector materials. Some of the most omnipresent and troublesome are ^{222}Rn and its daughters. Decay products from ^{222}Rn plate out on detector surfaces and have typically been assumed to be fixed there. In this chapter, a series of experiments is described; the results provide evidence that radon daughters can dissolve in liquid xenon.

7.1 MOTIVATION

Radon and radon daughters produce problematic backgrounds for rare-event searches [33]. Of particular concern for liquid xenon dark matter detectors are “naked” beta decays. These ground-state to ground-state decays have no accompanying gammas and cannot be rejected via coincidence tagging. Rejection of these backgrounds in WIMP search experiments relies solely on being able to discriminate electron recoils from nuclear recoils. For example, the ER leakage fraction from the LUX Run03 tritium calibration is on the order of 2/1000 over the WIMP search region [34] (See Chapter ?? for more details). The ^{222}Rn chain contains ^{210}Pb ($T_{1/2} = 22.23$ y), effectively splitting the decay chain into a “fast chain” and “slow chain” (Fig. 34). Radon can be introduced via two pathways: (1) during detector construction and (2) during detector operation (see Fig. 35). Great care is taken to ensure minimal contamination via pathway 2 because the fast chain naked betas, ^{214}Pb and ^{214}Bi , may decay in the fiducial volume before the purification system can remove them or before they can plate out on detector surfaces. In pathway 1, ^{222}Rn and daughters plate out onto detector surfaces during construction of parts, and construction of the detector itself. Models for plate out can be found in [35] and [36]. Typically it is assumed that once ^{222}Rn and daughters plate out, they remain fixed at that position, and can be rejected by a fiducial volume cut. This means that the slow chain naked betas of ^{210}Pb and ^{210}Bi from initial exposure during construction are assumed to occur outside the fiducial volume. However, evidence of ^{210}Bi mobility has been

observed in the liquid scintillator environment of KamLAND [37], [38] and Borexino [39]. If radon daughters are soluble in liquid xenon, the late chain naked betas (from both pathway 1 and 2) pose a serious background distributed throughout the fiducial volume.

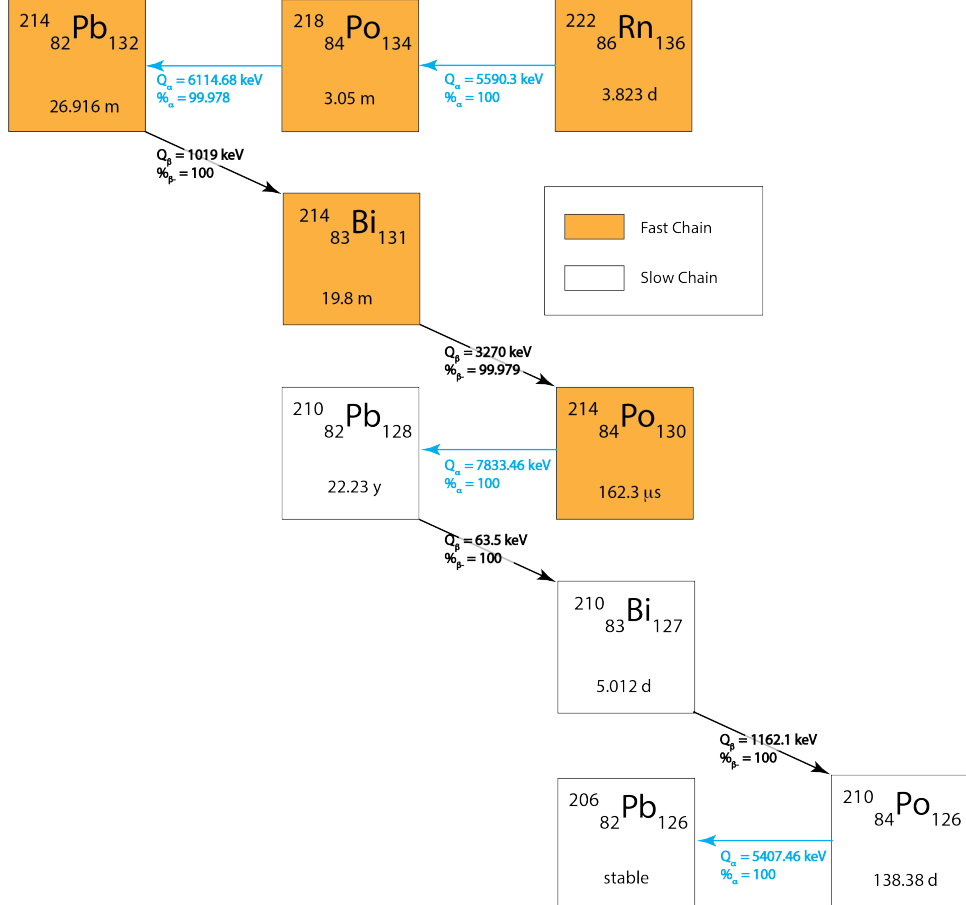


Figure 34: The ^{222}Rn decay scheme. The fast and slow chains are indicated.

In order to investigate the solubility of radon daughters in liquid xenon, a ^{220}Rn source was employed. The analogous long lived daughter in this chain, ^{212}Pb , has a half-life of 10.6 h, making it appropriate for a laboratory test. Investigating pathway 2 in the laboratory by introducing radon in a LXe environment will necessarily yield inconclusive results, because it is impossible to tell if the daughter decay of interest plated out before decaying. Therefore, we required the radon daughters to be on a surface.

Xenon gas was circulated through the ^{220}Rn source and detector components for a period of >24 h. The detector was then evacuated, thereby assuring the initial position of radon daughters on a detector surface. Any radon daughters subsequently observed in the bulk region after condensing liquid xenon must therefore have dissolved.

Pathways to Radon and Radon Daughters Contamination

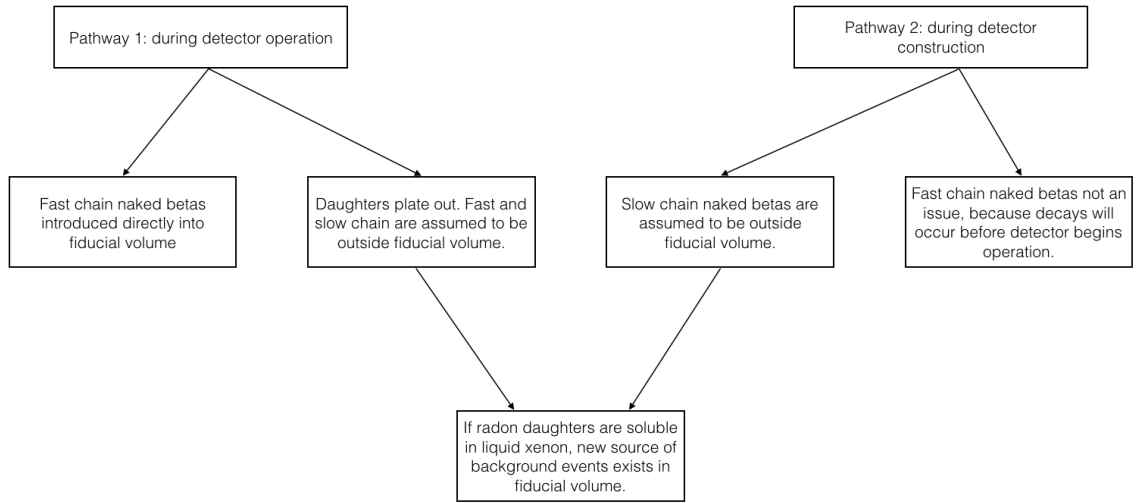


Figure 35: Pathways to radon and radon daughter contamination.

7.1.1 PLATE OUT

The term “plate out” is used above but not defined. The literature indicates that there two known types of radon daughter plate out [40]. The following terms are used in [40] to identify each type.

1. *implantation* Alpha recoil implantation of a daughter nucleus
2. *sticking* Daughters are sitting on the surface of a material, it is possible to wash a percentage of these off with various surface cleaning methods.

The percentages of daughters plated out in these different modes are not indicated, but [40] relates a story of researchers being unable to remove ^{214}Po from glass samples, where as ^{218}Po was easily removed with surface cleaning methods. This is explained by the fact that further down the ^{222}Rn chain, more alpha decays have occurred, so a late-state daughter has had more chance to be implanted. It is also noted that the durability of the implanted activity subject to change under different conditions, as is the implant integrity. The author cites factors such as humidity and temperature affecting whether daughters implant, and whether they remain implanted; since the conditions for plate out are different in pathways 1 and 2 and it logical to infer that implantation functions differently in these two environments for LXe TPCs.

The chemistry of radon has been studied as well, and may provide some context to the plate-out discussion. Radon is frequently regarded as a totally inert element. It is, however, classified as a “metalloid”, and exhibits some of the characteristics of both true metals and nonmetals. For example, it is known to react chemically with fluorine, halogen fluorides, dioxygenyl salts, fluoro-nitrogen salts, and halogen fluoride-metal fluoride complexes to form ionic compounds [41]. It is also known to co-crystallize with hydrogen chloride, hydrogen sulfide, sulfur dioxide and carbon dioxide [42]. In the latter case, the author notes that the radon is not forming true chemical bonds, but rather is held in place by weak Van der Waals forces. These chemical experiments found radon to be readily reactive at “room temperature and lower”, but the low temperate range is not stated. Chemical bonds formed by radon may make up a different type of plate out, or sub-type of ‘sticking’. Presumably weak surface Van der Waals forces belong in the ‘sticking’ type as well.

If we look to surface physics, the plate-out term ‘sticking’ is well defined by the terms physisorption and chemisorption. Physisorption is distinct from chemisorption in that it is a general phenomenon occurring between the adsorbed atom and surface, where chemisorption involves a chemical reaction between surface and adsorbate, and is characterized by higher bond strengths. Chemisorption potentials have been calculated for many atoms and surfaces [43] and are generally greater than 1 eV. Physisorption potentials, such as the well-known Van der Waals potential, are less than 1 eV and as low as 10 meV.

Plate out occurs with different rates on different materials [44], and can be an order of magnitude larger on PTFE than stainless steel, likely due to PTFE’s tendency to accumulate negative static charge [45]. Plate out of radon daughters can be reduced by employing a nitrogen gas purge or an electric field (approximately 90% of radon daughters are charged) [46]. However, [44], [45], and [46] do not distinguish between implantation and sticking, and only use the term “plate out”.

7.2 EXPERIMENTAL CONFIGURATION AND METHOD

A diagram of the TPC for this work is shown in Fig. 36. A 50 mm diameter cathode wire grid, extraction wire grid, and a planar, segmented anode were held in Teflon PTFE housing. The anode was instrumented with charge-sensitive preamplifiers. Both grids were constructed from a stainless steel frame strung with 4 μm diameter stainless steel wire on a 2 mm pitch. The xenon inlet was a PTFE tube which introduced xenon gas into the liquid region where it was condensed. The xenon liquid outlet was a thin stainless steel capillary that drew liquid from the TPC into the

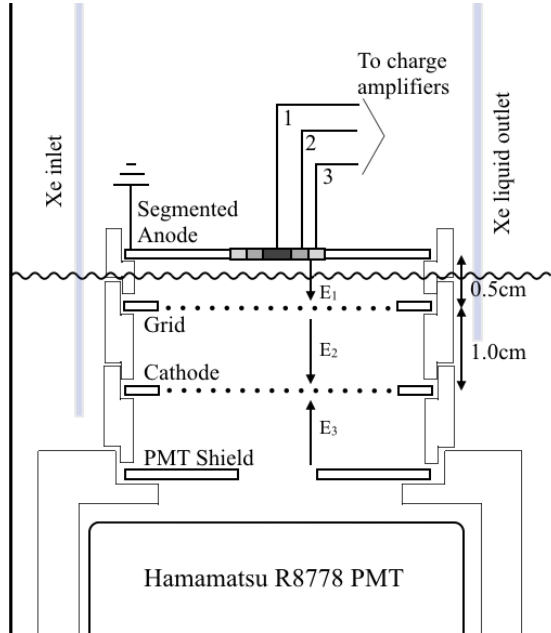


Figure 36: Diagram of the test bed. For this study, the cathode is held at -6.0 kV, and the grid is held at -4.0 kV. $E_1^{liq} \approx 5.0$ kV/cm, $E_1^{gas} \approx 10.0$ kV/cm $E_2 = 1.0$ kV/cm. $E_3 = 2.7$ kV/cm. The large gray regions represent the structural rings of PTFE. The line between the grid and anode represents the liquid xenon level. The xenon inlet pipes incoming gas directly into the liquid region, and the liquid outlet pulls from the level of the active region. A gas outlet (not pictured) also draws xenon gas into the circulation system to be purified.

purification system. Both inlet and outlet tubes were placed near holes drilled in the PTFE to aid circulation into the active volume.

A particle interaction in the liquid xenon volume produced primary scintillation photons (S1) and ionization electrons. The ionization electrons were drifted with an electric field into the gas phase, where they produced secondary scintillation light (S2). A single Hamamatsu R8778 VUV-sensitive PMT was installed in Teflon PTFE housing, facing upward to view the active region. Directly above the PMT was a copper shield mask, held at the same voltage as the PMT bias of -1250 V.

The TPC was filled with 1.5 bar of xenon gas at room temperature. The gas was circulated continuously through the TPC and a heated zirconium getter for at least 24 hours to remove contaminants. The TPC was then cooled to -100° C while circulating xenon gas. Circulation was stopped, and xenon was condensed into the TPC until the liquid level rose to between the extraction grid and anode. The process of filling the TPC took 4 to 5 hours. The liquid level was kept stable by keeping the temperature and pressure constant in the TPC. During data collection, xenon from the

TPC was circulated through a getter and re-condensed into the TPC to remove impurities.

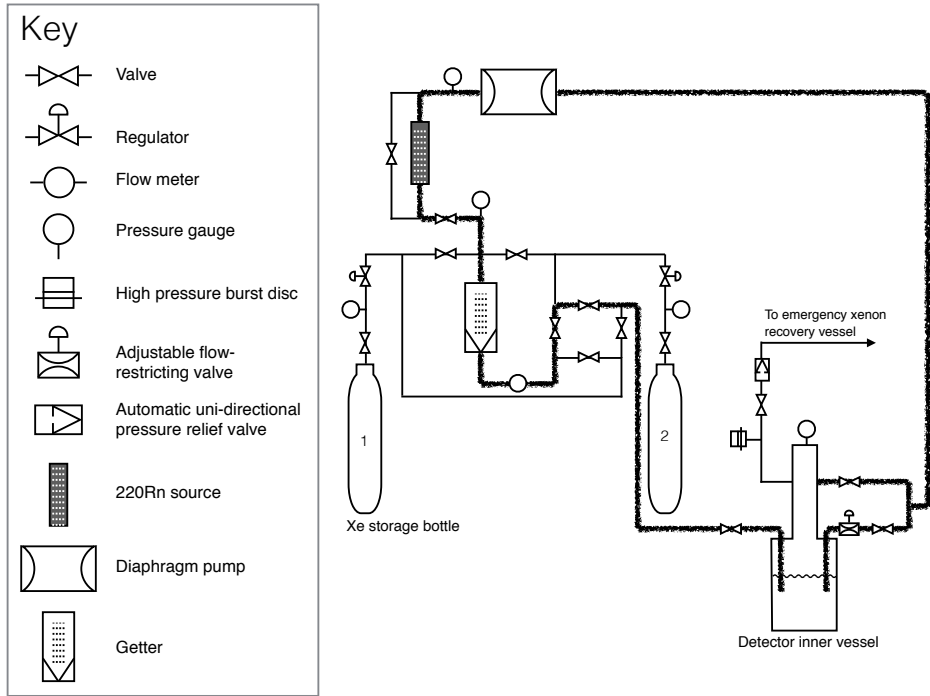


Figure 37: An example a circulation path used for plate out is shown on the pumping and instrumentation diagram. During data-taking the radon source was bypassed. The typical liquid level is indicated on the diagram to show that the outlet drew from the liquid via a capillary, ensuring purification of the liquid xenon. A gas purge also purified the gas column in the detector.

7.2.1 PLATE OUT OF ^{220}Rn DAUGHTERS

The procedure to plate out ^{220}Rn daughters on the inner surfaces of the detector was the same as described in Sec. ??, except that the circulation path was directed through a 2 kBq ^{220}Rn source. The ^{220}Rn is shown in Fig. 38. The rate of radon activity in the TPC was measured to be 4.5 ± 0.5 Hz during plate out. The total alpha rate was measured by taking repeated 1200 ms traces on an oscilloscope of the PMT with a falling edge trigger and counting the alpha decays. This rate was then halved to get the rate of radon decays. The 4.5 ± 0.5 Hz rate of radon activity represents activity for all of the space internal to the PTFE support structure. Decay daughters diffused until they contacted a wall or other surface, where they could plate out. Some percentage of decay daughters are expected to be positively charged ions. If the cathode grid was biased, charged decay

daughters drifted preferentially to the cathode grid. The cathode voltage during plate outs is noted in Table 1.

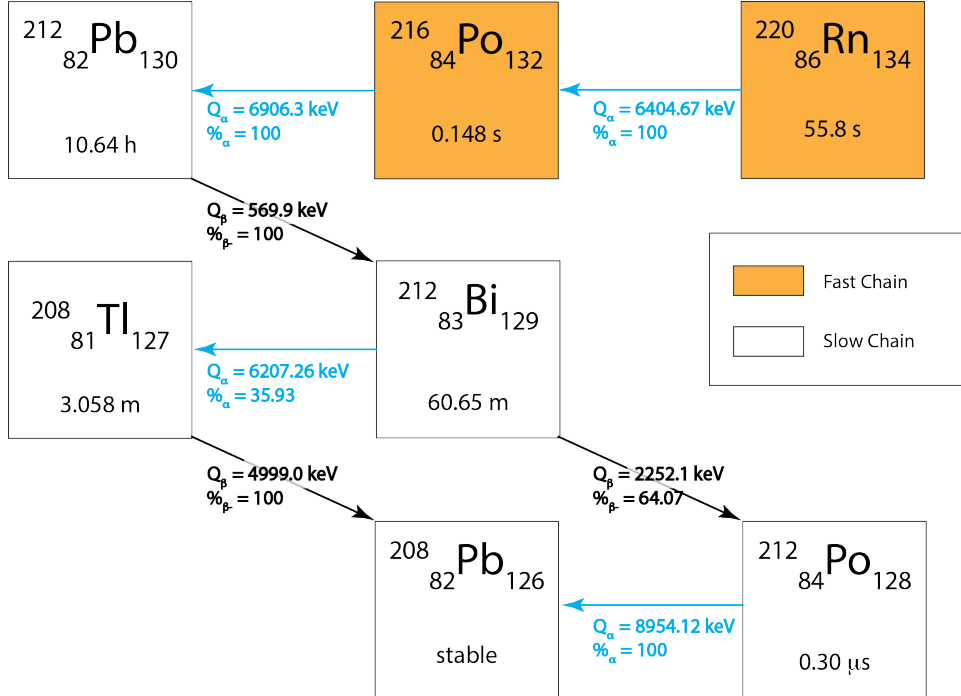


Figure 38: The ^{220}Rn decay scheme. The fast and slow chains are indicated. Events in the plate out data sets are from the slow chain.

Prior to filling the TPC with liquid xenon, the circulation was stopped and the xenon gas removed from the TPC and the circulation lines. A vacuum pressure of a few 10^{-4} Torr was achieved in a period of ten minutes. This step ensured removal of ^{220}Rn and decay daughters which are dissolved in the gas, leaving only those daughters which had plated out on a detector surface. Since the fill time of the TPC is 4 to 5 hours, there were no fast chain alpha decays of ^{220}Rn and ^{216}Po in the plate out data. Additional details are summarized in Table 1.

7.2.2 DATA COLLECTION

Voltage records from PMT and charge channels were collected with a 14-bit ADC with 125 MHz sampling and a 20 MHz low-pass filter. The trigger was a coincidence between the PMT and the central anode segment, used to select events in the central ($r < 3$ mm) column of xenon. This avoids any electric field fringing effects.

	dataset ID	A	B	C	D
Plate-Out	Circ thur ^{220}Rn Source	yes	yes	no	-
	Circulation Time (h)	24	48	24	-
	Cathode Voltage (kV)	-1	0	0	-
Data-Taking	Circ thur ^{220}Rn Source	no	no	no	yes
	Cathode Voltage (kV)	-6	-6	-6	-6
	Grid Voltage (kV)	-4	-4	-4	-4
Livetime (h)		12.02 ± 0.5	23.93 ± 0.5	25.02 ± 0.2	4.15 ± 0.2

Table 1: Summary of plate out and data-taking conditions. Data sets A and B are taken after circulating radon gas and data set C, background, had no radon circulation. Data set D was taken following dataset A, and radon was circulated in a liquid xenon environment, purposefully introducing radon into the detector bulk to calibrate the detector.

7.2.3 CALIBRATION

In order to identify a signal region for bulk radon daughters, the flow through ^{220}Rn source was employed directly following dataset A, allowing ^{220}Rn to flow into the liquid bulk of the TPC. The bulk daughter decay of interest, ^{212}Bi alpha, has an energy approximately equal to the ^{220}Rn alpha decay. The alpha signals were sufficient to saturate the biasing circuit of the PMT, so alpha decays within 1 MeV of each other were indistinguishable. Therefore, the region in S1 area vs. S2 area where the ^{220}Rn alphas appeared was also where ^{212}Bi alphas were expected (Fig. 43).

7.2.4 POSITION RECONSTRUCTION

The central anode segment was assumed to select events from the central column with 100% efficiency. Events occurring under one of the outer concentric segments can produce a signal on the central anode, but the signal was largest at the anode nearest the charge. It was not required that there be zero signal on the outer segments, so the (x,y) position of the event is treated as a source of uncertainty, which is taken into account in the calculation of fiducial volume. The drift time of the events was

calculated from the time difference between the S1 and S2 pulses, and a linear scaling of 2 mm/us was applied using the Miller (1968) electron drift velocity in LXe measurements.

7.2.5 FIDUCIAL VOLUME

Different values for the fiducial volume are presented below.

Anode Segments	1	2	3	Full
Radius (mm)	3	6	9	24
Area (mm ²)	28	113	255	1810
Volume (mL)	0.39 ± 0.03	1.6 ± 0.1	3.6 ± 0.3	25.3 ± 1.8
Mass (g)	1.1 ± 0.1	4.6 ± 0.3	10 ± 1	73.4 ± 5.2

Table 2: Calculations of fiducial volume. Liquid level is taken to be 14 ± 1 mm. Density of LXe near boiling point is 2.9 g/mL.

7.3 ANALYSIS

7.3.1 NUMBER OF ^{220}Rn DAUGHTERS IN THE TPC

As described in Sec. 7.2.1, the rate of ^{220}Rn in the TPC was measured to be 4.5 ± 0.5 Hz during plate out. From this, the number of daughter atoms ^{212}Pb and ^{212}Bi present in the TPC just prior to filling the liquid xenon were calculated. The number of daughter atoms as a function of the plate out time is shown in Fig. 39 along with the data acquisition periods for each dataset. This calculation assumes that the diffusion time in the PTFE walls was less than removal time via the capillary.

7.3.2 DATA SELECTION

The trigger described in Sec. 7.2.2 captured the slow chain decays as shown in Fig. 38. The ^{212}Bi beta decay is followed by the 300 ns alpha decay of ^{212}Po ; these decays are referred to herein as “Bi-Po”.

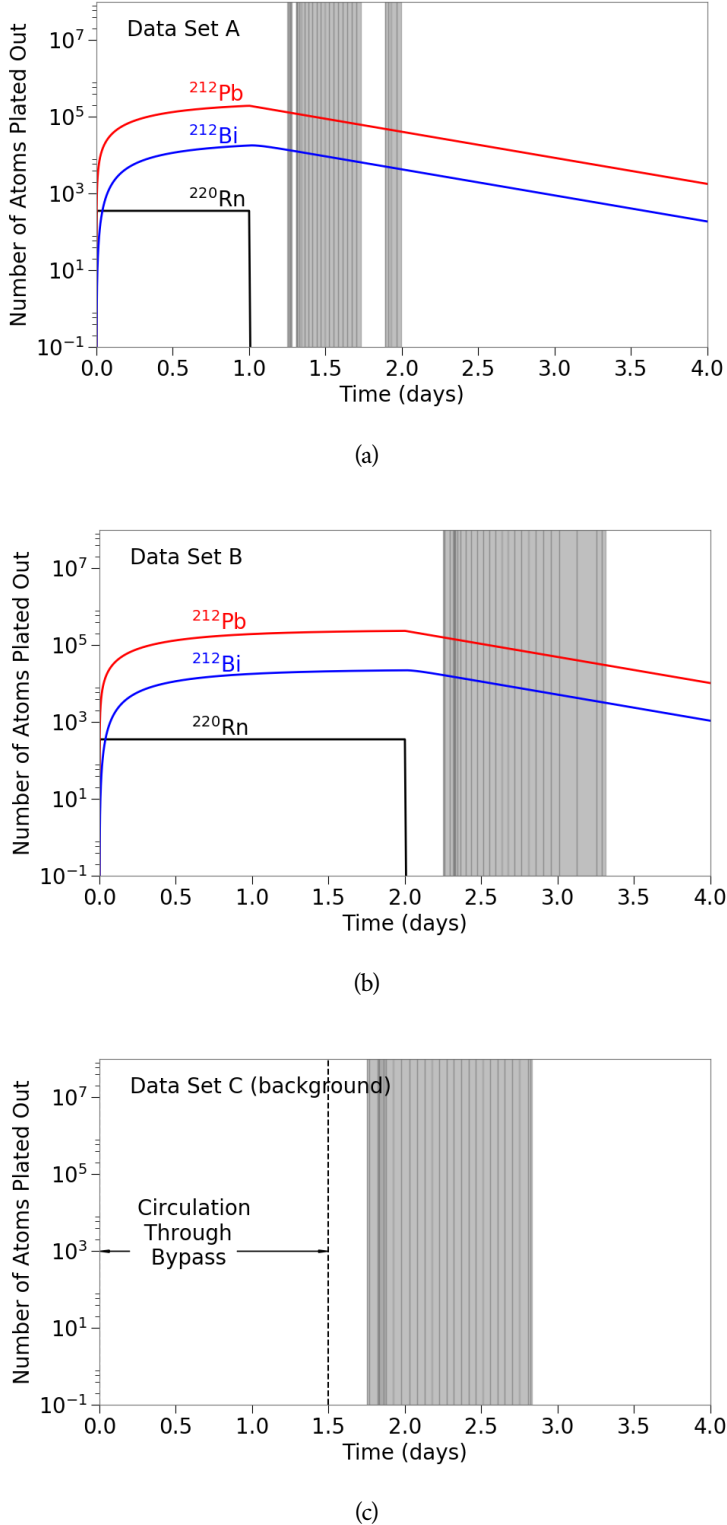


Figure 39: a) and (b) and (c) show the plateout conditions of datasets A, B, and C, respectively. The gray bands indicate time when data was being acquired. Dataset D (calibration) was taken following dataset A and consisted of a few hours.

The aim of this analysis was to reconstruct the z-position of radon daughter alpha decays via the timing difference between the S1 and S2 of an event. Therefore, Bi-Po events were rejected, as the two S2s presented a timing ambiguity. The focus was instead on identifying ^{212}Bi alpha decays. All events were expected to take place on detector surfaces, so ^{212}Bi alpha decays in the drift region indicate mobility of plated-out daughters ^{212}Pb and/or ^{212}Bi ; it was not possible to determine whether the original position was on the cathode wires, PTFE walls, or other detector surface.

The software cuts used to select ^{212}Bi alphas are described below:

1. **Data Cleaning** Remove events with any railed charge channel.
2. **Fiducialization** Require more signal in the central anode segment than the other two concentric anode segments.
3. **Select Alpha Events** The tallest pulse in an event was required to be an S1. Alphas are higher energy than the other decays in the ^{220}Rn chain, and have a characteristically high light yield, so this cut is generous in keeping all alpha events.
4. **Reject Bi-Po Topology** Of the alpha events, those with one S1 and one S2 (single-scatter) were classified as ^{212}Bi alpha. Events with two S1s (one of which is alpha-like), and one or two S2s were classified as Bi-Po.
5. **Reject Bi-Po Energy** There are two ways a Bi-Po event can mimic the topology of ^{212}Bi alpha: (i) alpha decay was prompt and so the scintillation signals from the beta and alpha were combined into one large S1 (ii) the beta was ejected into the cathode wire and therefore there was no signal detectable from the beta. To robustly identify ^{212}Bi , the alpha S1 areas of ^{212}Bi alpha and Bi-Po events from Step 2 were histogrammed and fit with Gaussian functions. ^{212}Bi alpha events were tightly selected with a high and low S1 area cut placed on single-scatter alpha events: anything above $(\mu - 3\sigma)_{\text{Bi-Po}}$ was considered a Bi-Po event and anything below $(\mu + 3\sigma)_{\text{Bi-alpha}}$ was considered a beta or gamma, and discarded (Fig. 40). It should be noted that this cut doesn't affect the signal region for ^{212}Bi alpha in bulk; it affects the region for ^{212}Bi alpha on the cathode. This cut is conservative in discarding Bi-Po events, as this leads to a more conservative fraction for dissolved fraction of ^{212}Bi alphas.
6. **Z-position Cut** Events in the cathode region were separated from events in the bulk region with a z-position cut (discussed further below).

7. **Bulk Signal Area Cut** Only ^{212}Bi alpha tagged events which also fell in a signal region expected from calibration with the ^{220}Rn flow though source (Fig. 43h) were considered to be daughters which have dissolved.

In order to choose the value for the z-position cut in Step 4, a Monte Carlo approach was used. A Bi-Po decay with a prompt alpha (appears as single-scatter) where the beta penetrates into the bulk region, could mimic a ^{212}Bi alpha bulk event. To better understand Bi-Po cathode events and the danger of mis-identifying them as ^{212}Bi alphas in bulk, a Monte Carlo study was done with the ^{212}Bi beta spectrum (the highest energy beta in the ^{220}Rn chain) to determine the maximum distance a beta could penetrate into the bulk region. The study yielded a maximum beta penetration of $z_{max,MC} = 0.12$ cm, see Fig. 41. The z position cut separating cathode from bulk was then defined to be $z_{cut} = z_{max,MC} + 3\sigma_{fit}$, where σ_{fit} is just the width of a Gaussian fit for the position of the cathode. Figures 42a and 42c show the cathode position fits as well the the location of z_{cut} . The cathode position fit error, σ_{fit} , was the same for both datasets A and B, and was also used to determine z_{cut} for the background and calibration sets.

One feature that merits further discussion from Figure 42 is the strong anti-correlation in S1 Pulse Area vs. S2 Pulse Area apparent in cathode events. The cathode region was subject to very high, non-uniform fields due to the thin wires that comprised the cathode grid. Events that occurred on the wires encountered different fields depending on their position on the surface of the wire. Additionally, two events that occurred at exactly the same spot encountered different fields depending on which direction the decay particle (alpha, beta, etc.) traveled. The amount of scintillation and ionization from an interaction in liquid xenon depends on the field at the interaction site. Higher fields result in more ionization electrons being separated from the interaction site and therefore more S2. Mono-energetic events occurring in a uniform field have small anti-correlated fluctuations in S1 and S2 size. Non-uniform fields greatly exaggerate the typical variation in S1 and S2 size resulting in the spread out cathode region (blue) observed in Figures 42 and 43 (right). Events in the bulk region encounter a relatively low, uniform field resulting in a compact signal region in S1 vs. S2 (visible in red region of calibration data, Dataset D).

7.4 RESULTS AND DISCUSSION

We observed 11 bulk ^{212}Bi alphas for dataset A, 20 for dataset B, and 1 background event in the signal region from dataset C. The counts of cath-

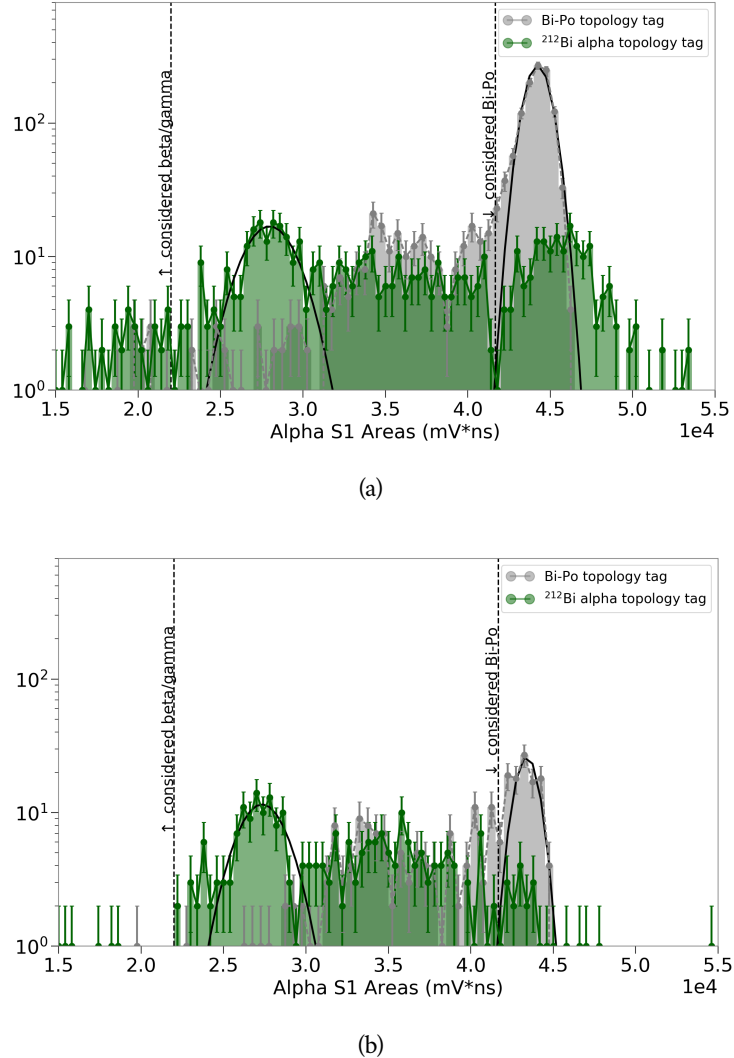


Figure 40: The S1 areas of events that were tagged using topological features.

These distributions were then used to employ the cuts in Step 3. The branching ratio for ^{212}Bi is 36:64 for α :Bi-Po. Dataset (a) showed 10:90 and dataset (b) showed 35:65. It is unclear why the branching ratios for dataset (a) deviate so much from expectation. The trigger is more efficient for Bi-Po events because those decays would produce more a larger charge signal. It's possible that the cathode being left on during the plate out procedure had some effect on the geometrical distribution of daughters on the cathode wires, which further biased the trigger.

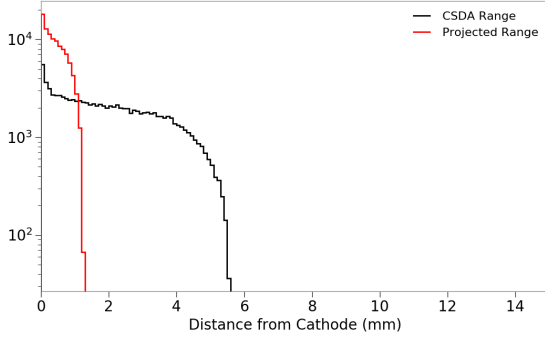


Figure 41: Monte Carlo study to find the maximum distance a ^{212}Bi beta (2.2 MeV) on the cathode could penetrate into the drift region. The projected range (red) is the relevant curve for this analysis; it shows a beta is not expected to travel more than 1.2mm from the cathode.

ode region ^{212}Bi alphas are presented in Table 3. There was only one background event observed in the signal region, so with 95% confidence the true background count is at most 4.74. The observed counts for dataset A and B lie far above the 95% confidence limit for background, indicating they are true observations of ^{212}Bi alphas in bulk. Defining dissolved fraction as N_{bulk} / N_{cath} , the dissolved fraction of ^{212}Bi alphas for dataset A (≈ 13 h livetime) is 0.035 ± 0.010 , and for data set B (≈ 25 h livetime) is 0.099 ± 0.020 .

These results indicate that either ^{212}Pb or ^{212}Bi itself is soluble to a small degree in liquid xenon.

Table 3: Number of detected alpha particle events whose energy determination was consistent with ^{212}Bi decay to ^{208}Tl . Live times are quoted in Table 1

dataset ID:	A	B	C
Bulk Events	11	20	1
Cathode Events	300	183	4

The solubility is presented in the following units:

$$\frac{\frac{Bq (dissolved)}{kg LXe}}{\frac{Bq (plated out)}{cm^2 (detector surface)}}$$

7.4 RESULTS AND DISCUSSION

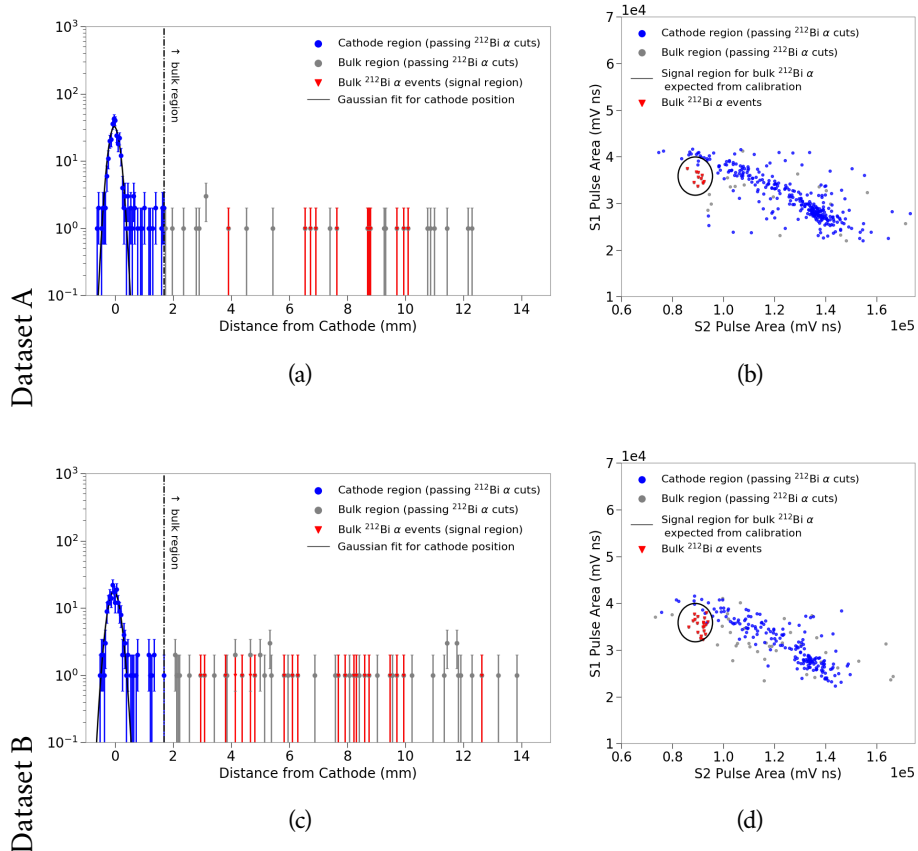


Figure 42: For datasets A and B: **(left)** Distribution of events in z . **(right)** The same events distributed in the S1-S2 plane, showing selection criteria for candidate ^{212}Bi alpha events in the bulk liquid xenon.

7.4 RESULTS AND DISCUSSION

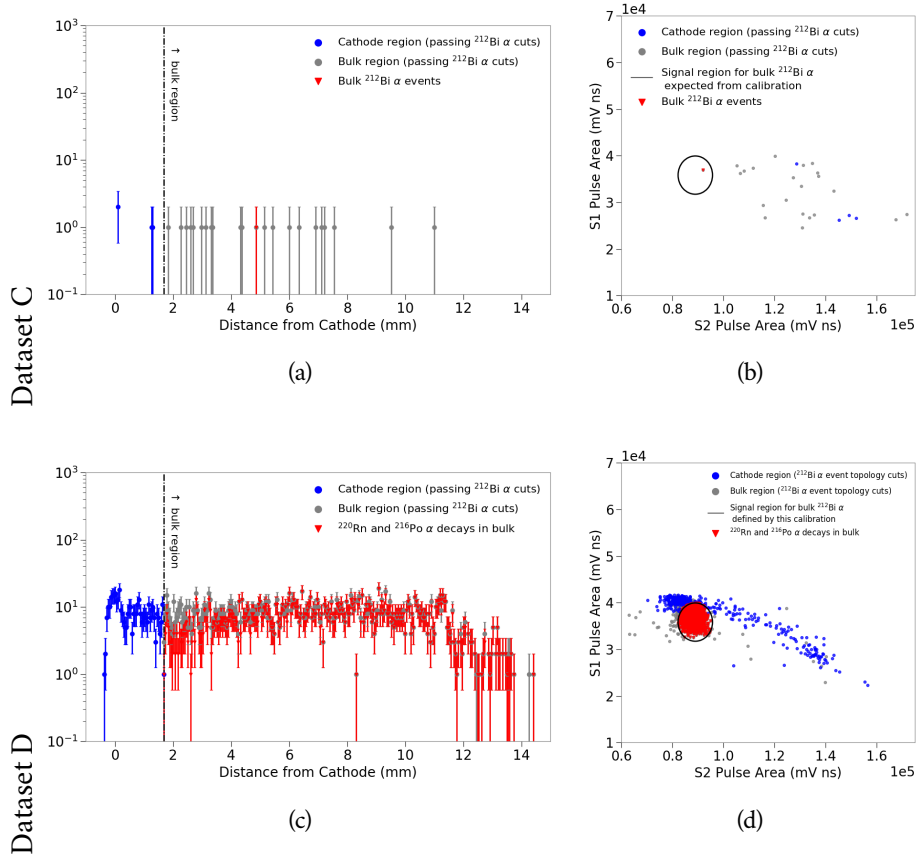


Figure 43: For datasets C and D: **(left)** Distribution of events in z . **(right)** The same events distributed in the S1-S2 plane, showing selection criteria for candidate ^{212}Bi alpha events in the bulk liquid xenon.

The solubility calculation is subject to errors from the following factors. Where appropriate, it is noted how the error taken into account in the calculation; otherwise, the assumption is stated.

1. Liquid height (folded into fiducial volume)
2. Area over which charge amps are sensitive (calculation using different fiducial volumes)
3. Area over which daughters are plated out (varying area over which ^{212}Bi is distributed; assume 10% error in area calculation)
4. Initial activity of plated out daughters (assume circulation time for gas to leave inner PTFE stack > decay time of ^{216}Po)
5. Live time calculation (uncertainty included)

The solubility found in dataset A is at worst $84 \pm 26 \text{ Bq/kg/Bq/cm}^2$ and at best $0.091 \pm 0.030 \text{ Bq/kg/Bq/cm}^2$. For dataset B, the worst case is $58. \pm 18. \text{ Bq/kg/Bq/cm}^2$ and the best case is $0.064 \pm 0.021 \text{ Bq/kg/Bq/cm}^2$.

These results are first evidence that the ^{220}Rn daughters ^{212}Pb and/or ^{212}Bi are soluble in liquid xenon. The dissolved events are a small fraction of events that are plated-out on detector surfaces. These daughters are proxies for the isotopes ^{210}Pb and/or ^{210}Bi , which undergo naked beta decays in the ^{222}Rn chain and pose a problem for liquid xenon dark matter detectors. Our study counts dissolved ^{212}Bi alpha events as well as ^{212}Bi alphas plated out on the cathode. We found 11 counts in dataset A and 20 counts in dataset B consistent with ^{212}Bi decay in the bulk region; these counts are significantly above a background count of 1. The experimental apparatus is not characterized extensively. Regardless, we carried through the solubility calculation, taking into account uncertainties to arrive at a ‘best case’ and ‘worst case’ result.

The limit derived from LUX observations, stated in the LZ projected sensitivity paper [47], is $0.1 \mu \text{Bq/kg LXe}$ for ^{212}Bi mobility, given 50nBq/cm^2 on PTFE panels. Our observed solubility is much greater than this. One explanation is that we are sensitive to the ‘stuck’ radon daughters that wash off easily in the first few days of an experiment due to the introduction of [LXe](#). Large TPCs may then expect an increased rate of radon daughter decays in the fiducial volume at the beginning of a search, but a decreasing rate as these are removed by the getter or are implanted in detector materials.

Another, testable, explanation that would reconcile the different solubilities in the ^{220}Rn and ^{222}Rn chain is beta ejection. Referring to Figures ?? and ??, both bottleneck decays, ^{XXX}Pb , are beta decays. However, ^{212}Pb in the ^{220}Rn chain has a beta decay endpoint of 570 keV, which

7.4 RESULTS AND DISCUSSION

about 10 times of the endpoint energy for ^{210}Pb in the ^{222}Rn chain. Daughter recoils from beta decay are indeed small; the endpoints are approximately 0.6 eV for the recoil from ^{212}Pb decay in the ^{220}Rn chain and 0.006 eV for the recoil from ^{210}Pb decay in the ^{222}Rn chain. The physisorption potential in for both cases is expected to be below 1 eV. Depending on the exact value, which is unavailable, the ^{212}Pb decay could provide enough energy to liberate the daughter ^{212}Bi most of the time, whereas ^{210}Pb decay produces a maximum recoil value below the potential depth.

Further study, where a known amount of ^{220}Rn daughters are plated out on a known area is necessary to measure dissolution rates. Additional studies that compare the solubility of radon daughters adsorbed on different materials, and under different conditions (e.g. temperature) would also be useful. The effect of cleaning these surfaces before searching for dissolved daughters should also be investigated.

If beta recoil, not ‘washing’ by the LXe , is the cause of radon daughter solubility, then the high rate seen by this study of ^{220}Rn can be reconciled with the low rate of ^{222}Rn daughter dissolution seen in large experiments.

7.4 RESULTS AND DISCUSSION

Table 4: Using observations from 3, proceed through solubility calculation.

dataset ID:	A	B
Total Inferred Bi decays	20 ± 6	36 ± 11
Livetime (hours)	12.02 ± 0.5	23.93 ± 0.5
μBq Bi in bulk	460 ± 140	420 ± 130
Bq (dissolved) / kg LXe (smallest fiducial)	0.42 ± 0.13	0.38 ± 0.12
Bq (dissolved) / kg LXe (largest fiducial)	0.0063 ± 0.0020	0.0057 ± 0.0018

Plate-Out Areas		
	Area	
Total Internal Area Including PMT	496 cm^2	
Active Region PTFE	36 cm^2	

dataset ID:	A	B
Number of ^{212}Bi Plated-Out	13191	17280
Bq (plated-out)	2.5	3.2
Bq (plated) / cm^2 min	0.0050 ± 0.0005	0.0065 ± 0.0007
Bq (plated) / cm^2 max	0.069 ± 0.007	0.089 ± 0.009

Solubility		
dataset ID:	A	B
Solubility min	0.091 ± 0.030	0.064 ± 0.021
Solubility max	$84. \pm 26.$	$58. \pm 18.$

8

ELECTRON TRAIN STUDIES

8.1 ELECTRON TRAIN STUDIES

8.1.1 MOTIVATION

8.1.2 EXPERIMENTAL CONFIGURATION

8.1.3 RESULTS

PART IV

APPENDIX

A

DUMMY APPENDIX

BIBLIOGRAPHY

- [1] D. S. Akerib et al. “Chromatographic separation of radioactive noble gases from xenon”. In: *Astropart. Phys.* **97**: (2018), pp. 80–87. issn: 09276505. arXiv: [1605.03844](https://arxiv.org/abs/1605.03844).
- [2] E. Aprile et al. “Removing krypton from xenon by cryogenic distillation to the ppq level”. In: *Eur. Phys. J. C* **77**:5 (2017). issn: 14346052. arXiv: [1612.04284](https://arxiv.org/abs/1612.04284).
- [3] Carl Eric Dahl. “The physics of background discrimination in liquid xenon, and first results from Xenon10 in the hunt for WIMP dark matter.” In: PhD Thesis (2009).
- [4] J. Mock, N. Barry, K. Kazkaz, D. Stolp, M. Szydagis, M. Tripathi, S. Uvarov, M. Woods, and N. Walsh. “Modeling pulse characteristics in Xenon with NEST”. In: *J. Instrum.* **9**:4 (2014). issn: 17480221. arXiv: [arXiv:1310.1117v2](https://arxiv.org/abs/1310.1117v2).
- [5] K. Abe et al. “XMASS detector”. In: *Nucl. Instruments Methods Phys. Res. Sect. A Accel. Spectrometers, Detect. Assoc. Equip.* **716**: (2013), pp. 78–85. issn: 01689002. arXiv: [1301.2815](https://arxiv.org/abs/1301.2815).
- [6] XMASS Collaboration. “A direct dark matter search in XMASS-I”. In: (2018), pp. 1–23. arXiv: [1804.02180](https://arxiv.org/abs/1804.02180). URL: <http://arxiv.org/abs/1804.02180>.
- [7] F. Neves, A. Lindote, A. Morozov, V. Solovov, C. Silva, P. Bras, J. P. Rodrigues, and M. I. Lopes. “Measurement of the absolute reflectance of polytetrafluoroethylene (PTFE) immersed in liquid xenon”. In: *J. Instrum.* **12**:1 (2017). issn: 17480221. arXiv: [1612.07965](https://arxiv.org/abs/1612.07965).
- [8] C Faham. “Prototype, Surface Commissioning and Photomultiplier Tube Characterization for the Large Underground Xenon (LUX) Direct Dark Matter Search Experiment”. In: PhD Thesis (2014).
- [9] M. Auger et al. “The EXO-200 detector, part I: Detector design and construction”. In: *J. Instrum.* **7**:5 (2012). issn: 17480221. arXiv: [1202.2192](https://arxiv.org/abs/1202.2192).
- [10] D. S. Akerib et al. “Signal yields, energy resolution, and recombination fluctuations in liquid xenon”. In: *Phys. Rev. D* **95**:1 (2017), pp. 1–12. issn: 24700029. arXiv: [1610.02076](https://arxiv.org/abs/1610.02076).
- [11] E. Aprile and T. Doke. “Liquid xenon detectors for particle physics and astrophysics”. In: *Rev. Mod. Phys.* **82**:3 (2010), pp. 2053–2097. issn: 00346861. arXiv: [0910.4956](https://arxiv.org/abs/0910.4956).

- [12] J Lindhard, V Nielsen, M Scharff, and P V Thomsen. “Integral equations governing radiation effects”. In: *Det Kgl. Danske Viden.* **33**:10 (1963). URL: <http://www.sdu.dk/bibliotek/materiale+efter+type/hostede+ressourcer/matfys>.
- [13] Peter Sorensen and Carl Eric Dahl. “Nuclear recoil energy scale in liquid xenon with application to the direct detection of dark matter”. In: *Phys. Rev. D - Part. Fields, Gravit. Cosmol.* **83**:6 (2011), pp. 1–6. ISSN: 15507998. arXiv: [1101.6080](https://arxiv.org/abs/1101.6080).
- [14] LUX Collaboration et al. “Low-energy (0.7-74 keV) nuclear recoil calibration of the LUX dark matter experiment using D-D neutron scattering kinematics”. In: (2016), pp. 1–24. ISSN: 15502368. arXiv: [1608.05381](https://arxiv.org/abs/1608.05381). URL: <http://arxiv.org/abs/1608.05381>.
- [15] J. D. Lewin and P. F. Smith. “Review of mathematics, numerical factors, and corrections for dark matter experiments based on elastic nuclear recoil”. In: *Astropart. Phys.* **6**:1 (1996), pp. 87–112. ISSN: 09276505. arXiv: [1410.6160](https://arxiv.org/abs/1410.6160).
- [16] Laura Baudis. “WIMP dark matter direct-detection searches in noble gases”. In: *Phys. Dark Universe* **4**: (2014), pp. 50–59. ISSN: 22126864. arXiv: [1408.4371](https://arxiv.org/abs/1408.4371). URL: <http://dx.doi.org/10.1016/j.dark.2014.07.001>.
- [17] V. Chepel and H. Araújo. “Liquid noble gas detectors for low energy particle physics”. In: *J. Instrum.* **8**:4 (2013). ISSN: 17480221. arXiv: [1207.2292](https://arxiv.org/abs/1207.2292).
- [18] U Oberlack. “First limits on WIMP dark matter from the XENON10 experiment”. In: *J. Phys. Conf. Ser.* **110**:6 (2008), p. 062020. ISSN: 1742-6596. URL: <http://stacks.iop.org/1742-6596/110/i=6/a=062020?key=crossref.bfd78c6898a820849cdc54a2974555a3>.
- [19] D. S. Akerib et al. “First results from the LUX dark matter experiment at the Sanford Underground Research Facility”. In: *Phys. Rev. Lett.* **112**: (2014). ISSN: 0031-9007, 1079-7114. arXiv: [arXiv:1310.8214](https://arxiv.org/abs/1310.8214). URL: <http://arxiv.org/abs/1310.8214>.
- [20] E. Aprile et al. “First dark matter results from the XENON100 experiment”. In: *Phys. Rev. Lett.* **105**:13 (2010), pp. 9–13. ISSN: 00319007. arXiv: [1005.0380](https://arxiv.org/abs/1005.0380).
- [21] P. Sorensen et al. “Lowering the low-energy threshold of xenon detectors”. In: *Proc. Sci.* (2010). ISSN: 18248039. arXiv: [arXiv:1011.6439v1](https://arxiv.org/abs/1011.6439v1).

- [22] Peter Sorensen. “Anisotropic diffusion of electrons in liquid xenon with application to improving the sensitivity of direct dark matter searches”. In: *Nucl. Instruments Methods Phys. Res. Sect. A Accel. Spectrometers, Detect. Assoc. Equip.* **635**:1 (2011), pp. 41–43. issn: 01689002. arXiv: [1102.2865 \[astro-ph.IM\]](https://arxiv.org/abs/1102.2865).
- [23] J. Angle et al. “Search for light dark matter in XENON10 data”. In: *Phys. Rev. Lett.* **107**:5 (2011), pp. 1–6. issn: 10797114. arXiv: [1104.3088](https://arxiv.org/abs/1104.3088).
- [24] Rouven Essig, Aaron Manalaysay, Jeremy Mardon, Peter Sorensen, and Tomer Volansky. “First direct detection limits on Sub-GeV dark matter from XENON10”. In: *Phys. Rev. Lett.* **109**:2 (2012), pp. 1–5. issn: 00319007. arXiv: [1206.2644](https://arxiv.org/abs/1206.2644).
- [25] D. S. Akerib et al. “A search for annual and diurnal rate modulations in the LUX experiment”. In: (2018), pp. 1–12. arXiv: [1807.07113](https://arxiv.org/abs/1807.07113). url: <http://arxiv.org/abs/1807.07113>.
- [26] D. S. Akerib et al. “First Searches for Axions and Axionlike Particles with the LUX Experiment”. In: *Phys. Rev. Lett.* **118**:26 (2017), pp. 1–7. issn: 10797114. arXiv: [1704.02297](https://arxiv.org/abs/1704.02297).
- [27] D. S. Akerib et al. “Calibration, event reconstruction, data analysis and limits calculation for the LUX dark matter experiment”. In: *Phys. Rev. D* **97**:10 (2017), p. 102008. issn: 24700029. arXiv: [1712.05696](https://arxiv.org/abs/1712.05696). url: <http://arxiv.org/abs/1712.05696>.
- [28] C. et al. (Particle Data Group) Patrignani. “Passage of Particles Through Matter”. In: *PDG* (2017). issn: 1434-6044. url: <http://dbcompas.ihep.su/2006/reviews/passagerpp.pdf>.
- [29] H. Bethe. “Zur Theorie des Durchgangs schneller Korpuskularstrahlen durch Materie”. In: *Ann. Phys.* **5**: (1930), pp. 325–400. issn: 15213889.
- [30] U Fano. “Penetration of Protons, Alpha Particles, and Mesons12”. In: *Ann. Rev Nucl. Scei* **123**: (1963), pp. 1–66. url: [https://www.google.com/books?hl=tr&lr={\&}id=I6wrAAAAYAAJ{\&}oi=fnd{\&}pg=PA287{\&}dq=Fano,+U.+ \(1964\).+Penetrations+of+protons,+alpha+particles,+and+mesons.+Studies+in+Penetra+tion+of+Charged+Particles+in+Matter,++1133 : 287 . +\(cited+on+pages+15 , +16 , +and+17 \) {\&}ots=PYmM1cE](https://www.google.com/books?hl=tr&lr={\&}id=I6wrAAAAYAAJ{\&}oi=fnd{\&}pg=PA287{\&}dq=Fano,+U.+ (1964).+Penetrations+of+protons,+alpha+particles,+and+mesons.+Studies+in+Penetra+tion+of+Charged+Particles+in+Matter,++1133 : 287 . +(cited+on+pages+15 , +16 , +and+17) {\&}ots=PYmM1cE).
- [31] Hans Bichsel. “A method to improve tracking and particle identification in TPCs and silicon detectors”. In: *Nucl. Instruments Methds Phys. Res. Sect. A Accel. Spectrometers, Detect. Assoc. Equip.* **562**:1 (2006), pp. 154–197. issn: 01689002.

- [32] J.H. Allison, W. W. M ; Cobb. "Relativistic Charged Particle Identification By Energy Loss". In: *Ann. Rev. Nucl. Part. Sci.* **30**: (1980), pp. 253–298.
- [33] D.S. Akerib et al. "Radiogenic and muon-induced backgrounds in the LUX dark matter detector". In: *Astropart. Phys.* **62**: (2015), pp. 33–46. ISSN: 09276505. arXiv: [1403 . 1299](https://arxiv.org/abs/1403.1299). URL: <http://dx.doi.org/10.1016/j.astropartphys.2014.07.009><http://linkinghub.elsevier.com/retrieve/pii/S0927650514001054>.
- [34] D. S. Akerib et al. "Tritium calibration of the LUX dark matter experiment". In: *Phys. Rev. D* **93**:7 (2016). ISSN: 24700029. arXiv: [1512 . 03133](https://arxiv.org/abs/1512.03133).
- [35] V. E. Guiseppe, S. R. Elliott, A. Hime, K. Rielage, and S. Westerdale. "A Radon Progeny Deposition Model". In: 2011, pp. 95–100. URL: <http://aip.scitation.org/doi/abs/10.1063/1.3579565>.
- [36] E. O. Knutson. "Radon and Its Decay Products in Indoor Air". Wiley, 1988.
- [37] Yasuhiro Takemoto. "7Be solar neutrino observation with KamLAND". In: *Nucl. Part. Phys. Proc.* **265-266**: (2015), pp. 139–142. ISSN: 24056014. URL: <http://linkinghub.elsevier.com/retrieve/pii/S2405601415003788>.
- [38] A. Gando et al. "Be 7 solar neutrino measurement with KamLAND". In: *Phys. Rev. C* **92**:5 (2015), p. 055808. ISSN: 0556-2813. URL: <https://link.aps.org/doi/10.1103/PhysRevC.92.055808>.
- [39] G. Bellini et al. "Final results of Borexino Phase-I on low-energy solar neutrino spectroscopy". In: *Phys. Rev. D* **89**:11 (2014), p. 112007. ISSN: 1550-7998. URL: <https://link.aps.org/doi/10.1103/PhysRevD.89.112007>.
- [40] Christer Samuelsson. "Plate-out and Implantation of 222Rn Decay Products in Dwellings". In: *Environ. Int. Vol.* **22**:Suppl. 1 (1996), pp. 839–843.
- [41] Lawrence Stein. "The Chemistry of Radon". In: *Radiochim. Acta* **32**: (1982), pp. 163–171. ISSN: 0036-8075.
- [42] Lawrence Stein. "Chapter 18 Chemical Properties of Radon". In: *Radon Its Decay Prod.* 1987, pp. 240–251.
- [43] J.K. Hammer, B; Norskov. "Theory of adsorption and surface reactions". In: (1997), pp. 285–351.
- [44] J . Bigu. "Plate-Out of Radon and Thoron Progeny on Large Surfaces". In: *Radon Its Decay Prod.* 1987. Chap. 21, pp. 272–284.

- [45] E S Morrison, T Frels, E H Miller, R W Schnee, and J Street. “Radon daughter plate-out onto Teflon.” In: *arXiv.org, e-Print Arch. Phys.* **090002**: (2017), pp. 1–4. ISSN: 15517616. URL: <http://arxiv.org/pdf/1708.08534.pdf>.
- [46] M. Bruemmer, M. Nakib, R. Calkins, J. Cooley, and S. Sekula. “Studies on the reduction of radon plate-out”. In: *AIP Conf. Proc.* **1672**: (2015). ISSN: 15517616. arXiv: [1506.04050](https://arxiv.org/abs/1506.04050).
- [47] D. S. Akerib et al. “Projected WIMP sensitivity of the LUX-ZEPLIN (LZ) dark matter experiment”. In: (2018), pp. 1–16. arXiv: [1802.06039](https://arxiv.org/abs/1802.06039). URL: [http://arxiv.org/abs/1802.06039](https://arxiv.org/abs/1802.06039).